




## Open Archive Toulouse Archive Ouverte (OATAO)

OATAO is an open access repository that collects the work of Toulouse researchers and makes it freely available over the web where possible

This is a Publisher's version published in: <http://oatao.univ-toulouse.fr/27636>

**Official URL:** <https://doi.org/10.1021/acs.jpcc.0c10417>

### **To cite this version:**

Torayev, Amangeldi and Engelke, Simon and Su, Zeliang and Marbella, Lauren E. and De Andrade, Vincent and Demortière, Arnaud and Magusin, Pieter C. M. M. and Merlet, Céline  and Franco, Alejandro A. and Grey, Clare P. *Probing and Interpreting the Porosity and Tortuosity Evolution of Li-O<sub>2</sub> Cathodes on Discharge through a Combined Experimental and Theoretical Approach.* (2021) *Journal of Physical Chemistry C*, 125 (9). 4955-4967. ISSN 1932-7447

Any correspondence concerning this service should be sent to the repository administrator: [tech-oatao@listes-diff.inp-toulouse.fr](mailto:tech-oatao@listes-diff.inp-toulouse.fr)

# Probing and Interpreting the Porosity and Tortuosity Evolution of Li-O<sub>2</sub> Cathodes on Discharge through a Combined Experimental and Theoretical Approach

Amangeldi Torayev, Simon Engelke, Zeliang Su, Lauren E. Marbella, Vincent De Andrade, Arnaud Demortière, Pieter C. M. M. Magusin, Céline Merlet, Alejandro A. Franco, and Clare P. Grey\*

Cite This: *J. Phys. Chem. C* 2021, 125, 4 495–4967

Read Online

ACCESS |

Metrics & More

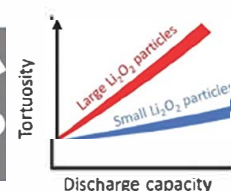
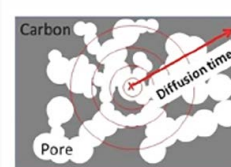
Article Recommendations

Supporting Information

**ABSTRACT:** Li O<sub>2</sub> batteries offer a high theoretical discharge capacity due to the formation of light discharged species such as Li<sub>2</sub>O<sub>2</sub>, which fill the porous positive electrode. However, in practice, it is challenging to reach the theoretical capacity and completely utilize the full electrode pore volume during discharge. With the formation of discharge products, the porous medium evolves, and the porosity and tortuosity factor of the positive electrode are altered through shrinkage and clogging of pores. A pore shrinks as solid discharge products accumulate, the pore clogging when it is filled (or when access is blocked). In this study, we investigate the structural evolution of the positive electrode through a combination of experimental and computational techniques. Pulsed field gradient nuclear magnetic resonance results show that the electrode tortuosity factor changes much faster than suggested by the Bruggeman relation (an equation that empirically links the tortuosity factor to the porosity) and that the electrolyte solvent affects the tortuosity factor evolution. The latter is ascribed to the different abilities of solvents to dissolve reaction intermediates, which leads to different discharge product particle sizes: on discharging using 0.5 M LiTFSI in dimethoxyethane, the tortuosity factor increases much faster than for discharging in 0.5 M LiTFSI in tetraglyme. The correlation between a discharge product size and tortuosity factor is studied using a pore network model, which shows that larger discharge products generate more pore clogging. The Knudsen diffusion effect, where collisions of diffusing molecules with pore walls reduce the effective diffusion coefficients, is investigated using a kinetic Monte Carlo model and is found to have an insignificant impact on the effective diffusion coefficient for molecules in pores with diameters above 5 nm, *i.e.*, most of the pores present in the materials investigated here. As a consequence, pore clogging is thought to be the main origin of tortuosity factor evolution.

kMC & PNM simulations

PFM-NMR



## INTRODUCTION

Lithium oxygen (Li O<sub>2</sub>) batteries are potentially game changing energy storage systems with a very high theoretical capacity,<sup>1</sup> but they face a wide spectrum of very significant material challenges that need to be overcome before achieving commercialization.<sup>2</sup> A Li O<sub>2</sub> battery consists of a lithium containing anode (typically Li metal), a separator soaked with an ionically conducting but electronically insulating electrolyte containing lithium ions (Li<sup>+</sup>), and a porous electronically conducting cathode (typically a porous carbon) in contact with oxygen gas. During discharge, lithium is oxidized at the anode and lithium ions migrate to the cathode where they react with oxygen (dissolved in the electrolyte) to form solid discharge products, predominantly Li<sub>2</sub>O<sub>2</sub> (lithium peroxide). During charge, Li<sub>2</sub>O<sub>2</sub> discharge products decompose and form Li<sup>+</sup> and O<sub>2</sub>. The lithium ions migrate back to the anode where they are reduced. Oxygen molecules are released back to the oxygen gas source. The predominant discharge product, Li<sub>2</sub>O<sub>2</sub>, is an electronic insulator.<sup>3</sup> During discharge, Li<sup>+</sup> reacts with O<sub>2</sub> to form LiO<sub>2</sub> (lithium superoxide) close to the cathode surface. LiO<sub>2</sub> can then form Li<sub>2</sub>O<sub>2</sub> via further electrochemical

reduction or through disproportionation. The growth of Li<sub>2</sub>O<sub>2</sub> can be further divided into two processes.<sup>4</sup> If the intermediate species, LiO<sub>2</sub>, is insoluble in the electrolyte, it is either directly reduced or it disproportionates to form a film of Li<sub>2</sub>O<sub>2</sub> on the cathode surface. The thickness of this film is limited by the electron tunneling through Li<sub>2</sub>O<sub>2</sub> leading to thin films of about 10 nm.<sup>5</sup> If the solubility of LiO<sub>2</sub> in the electrolyte is high, LiO<sub>2</sub> molecules can diffuse away from the carbon surface forming large, toroidal shaped discharge products via a disproportionation mechanism, which leads to pore clogging and impedes further transport of mobile molecules and ions in the electrolyte.<sup>6–8</sup>

Received: November 19, 2020

Revised: February 10, 2021

Published: February 25, 2021



In a Li O<sub>2</sub> cell, even though the active cathode (or positive electrode) material is oxygen, additional material is used to provide electronic conductivity and mechanical support to host the Li<sub>2</sub>O<sub>2</sub> discharge products. This support structure is typically a porous carbon and is also designated as being a part of the cathode, although in principle it is not electrochemically active. The choice of carbonaceous cathode material and its structure has a large impact on the performance of the cell. There are two main capacity limiting processes associated with the carbon cathode mesostructure. The first one is the passivation of the carbon surface area with electronically insulating discharge products,<sup>9–12</sup> and the second one is the slow transport of reactants, particularly oxygen, through the porous network.<sup>13–16</sup>

The passivation issue has been demonstrated at the experimental level in several studies as follows: Laoire *et al.*<sup>9</sup> studied it through cyclic voltammetry and rotating disc electrode characterization and Albertus *et al.*<sup>10</sup> through a combination of experimental and modeling techniques. One approach to mitigate passivation is to use a cathode with an extremely high surface area such as graphene based<sup>17,18</sup> or nanostructured electrodes.<sup>19</sup> Another strategy is to avoid the formation of passivating thin films by preferentially forming large discharge products through dissolution of the intermediate species. Selecting electrolyte solvents with high donor numbers<sup>20–23</sup> or choosing specific salt anions<sup>24</sup> can enhance the solubility of these intermediate discharge products and lead to large discharge product particles. Adding a small amount of water<sup>25,26</sup> or redox mediators<sup>27–29</sup> can also lead to the formation of large discharge product particles. While all of these methods reduce surface passivation, the formation of large discharge product particles often clogs the cathode pores, introducing new issues for reactant transport during electrochemical charge and discharge.

Transport limitations arise from a combination of the slow diffusion of oxygen and Li<sup>+</sup> in the electrolyte and the tortuous nature of the porous cathode. Using electrolytes with high oxygen diffusion coefficients,<sup>30,31</sup> and designing cathodes with high porous volume, and short and numerous diffusion pathways<sup>32–34</sup> can help in obtaining better battery performance. Regardless of the type of cathode mesostructure selected, the porous medium changes along discharge due to the formation of solid discharge products: some pores get smaller and some pores get clogged, impeding the transport processes<sup>13–16</sup> and motivating studies to investigate how the porous media change along discharge.

Bardenhagen *et al.*<sup>14</sup> investigated pore clogging for three gas diffusion electrodes along discharge using a three electrode electrochemical impedance spectroscopy setup. They identified four processes with different time constants, which they attributed to lithium ion migration through a surface layer, charge transfer from the carbon to the molecular oxygen, lithium and oxygen ion diffusion toward the cathode surface, and lithium ion movement inside the pores. Their observations confirmed that the pore clogging is a key limiting factor. In addition, they studied xerogel electrodes and showed that they provide high capacities due to the large volume of mesopores allowing for an improved oxygen transport.

To improve the battery performance, studies that directly investigate the transport properties, particularly tortuosity factor of the electrodes, are needed. Here, we present a work that focuses on the tortuosity factor evolution along discharge and investigate how it is affected by the type of electrolyte

used. For this purpose, pulsed field gradient nuclear magnetic resonance (PFG NMR) experiments are used. PFG NMR spectroscopy represents a powerful tool to measure diffusion of mobile species in porous media, which has been used to study ion transport in batteries and supercapacitors.<sup>35,36</sup> Forse *et al.* studied the effect of the pore size distribution on the self diffusion of ions and measured diffusion in and out of the nanopores in YP50F and YP80F, two porous carbon materials used in supercapacitors. <sup>1</sup>H, <sup>19</sup>F, and <sup>13</sup>C NMR experiments were conducted.<sup>35</sup> It was shown that the diffusion of ionic species is more than two orders of magnitude slower in nanoporous materials compared to diffusion in the bulk electrolyte. The ionic concentration, which changes along charge and discharge in the supercapacitor systems, also influences diffusion. Engelke *et al.*<sup>36</sup> used <sup>1</sup>H and <sup>7</sup>Li PFG NMR to measure anisotropic diffusion in model porous silicon substrates. They measured effective diffusion coefficients with incremental diffusion times, which allowed them to calculate the related mean square displacements and extract information about the pore dimensions. Stallmach *et al.*<sup>37</sup> and Kondrashova *et al.*<sup>38</sup> studied anisotropic self diffusion in nanoporous materials to analyze orientation dependent diffusivities, monitoring and quantifying diffusion of probe molecules along one dimensional channels.

In this work, we use <sup>1</sup>H PFG NMR to study the tortuosity factor evolution when discharging Super P cathodes in Li O<sub>2</sub> batteries. We focus on long range diffusion and measure effective diffusion coefficients of tetraglyme molecules in cathodes at different states of discharge. The tortuosity factor is computed from the ratio between the measured effective diffusion coefficient in the porous medium and the bulk diffusion coefficient. To study the effect of the solvent, we conduct experiments with two different electrolytes consisting in LiTFSI dissolved in either tetraethylene glycol dimethyl ether (tetraglyme) or in dimethoxyethane (DME). The tortuosity factor measurements are compared to tomographic imaging experiments on the discharged samples. To help interpret the experimental observations, we investigate the effect of pore sizes, and pore clogging, on the tortuosity factor, using a kinetic Monte Carlo (kMC) model and pore network model (PNM), respectively, as described in previous publications.<sup>39,40</sup>

## METHODOLOGY

**Cell Components Preparation. Anode.** A lithium metal anode is used in the eight cells of this study. The lithium anode is cut in a disk shape with a 0.73 mm thickness and 9 mm diameter. Considering that the density of lithium metal is 0.534 g cm<sup>-3</sup>, this negative electrode is sufficient to provide a capacity of about 95.8 mA h (7725 mA h g<sup>-1</sup>, normalized to cathode mass) per cell, which ensures that the anode is not a capacity limiting parameter, as none of the cells reached this high discharge capacity.

**Separator.** Two layers of Whatman glass fiber with a diameter of 14 mm are used in each cell. The total thickness of these two layers is about 1 mm. Two layers are used to avoid any short circuit in the cell assembly.

**Electrolyte.** Two different solvents are used, dimethoxy ethane (DME, anhydrous 99.5%, Sigma Aldrich) and tetraethylene glycol dimethyl ether (tetraglyme, 99%, Acros Organic). LiTFSI (lithium bis(trifluoromethanesulfonyl)imide, Sigma Aldrich) was used as a salt. Before use, the salt was dried

in a vacuum oven at 120 °C overnight and transferred into an argon glovebox.

**Cathode.** Self standing mesoporous Super P carbon electrodes were prepared from a mixture of 70% (mass percentage) Super P carbon (TIMCAL) and a 30% PTFE (polytetrafluoroethylene) binder in ethanol. The mixture was agitated using magnetic stirring at 70 °C for about 2 h, and the resulting paste was rolled into an approximately 300  $\mu\text{m}$  thick film. The film was cut into electrodes with diameters of 11 mm. After initial drying of the electrodes in a 50 °C oven under ambient air, they were further dried under vacuum at 120 °C for 12 h. The dried electrodes were taken into an argon gas glovebox without air exposure and then used to make batteries. The mass loading of the electrode is around  $13.0 \pm 0.4 \text{ mg cm}^{-2}$  (around 9.1  $\text{mg cm}^{-2}$  of carbon mass loading, 70 wt%). The discharge capacities reported in this article are normalized by the total electrode mass (12.4 mg: mass of binder + carbon).

**Electrochemical Testing and Sample Preparation for PFG-NMR and Tomography.** For the electrochemical experiments, Swagelok cells are used (Figure 1a). A hole was

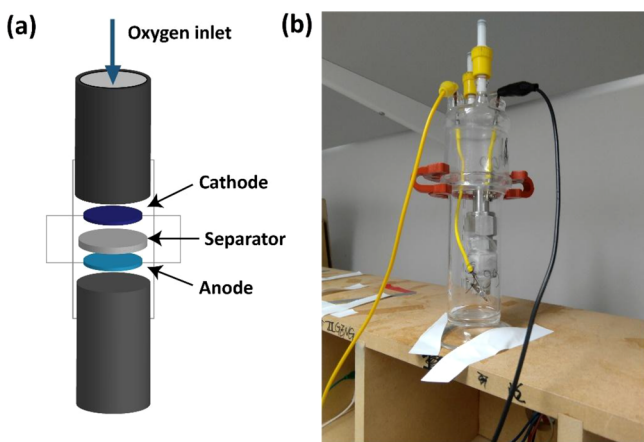


**Figure 1.** (a) Scheme of the Swagelok cell used for the electrochemical experiments. (b) The glass chamber used to keep the Swagelok cells under oxygen, which has space for a single Swagelok cell.

drilled through the plunger at the cathode side to connect to the oxygen supply. A lithium metal anode, two layers of separators, and a cathode were placed into the cell; then 250  $\mu\text{L}$  of electrolytes was added. The cell was assembled in an argon glovebox and put into an airtight glass chamber (Figure 1b). Once the glass chamber was sealed, it was taken out of the glovebox and flushed with oxygen gas for 5 min to replace the argon gas with oxygen. After flushing and before the electrochemical tests, the cell was rested for 6 h to give a sufficient time for oxygen molecules to dissolve in the electrolyte.

The electrochemical tests have been carried out on a Bio Logic VMP3 multichannel potentiostat. Four cells with 0.5 M LiTFSI in tetraglyme and four cells with 0.5 M LiTFSI in DME electrolytes were discharged galvanostatically with a current of 50  $\mu\text{A}$ . The discharge process was stopped at different depths of discharge for the different cells, the Swagelok cells were disassembled, and the cathode mesostructures were analyzed by PFG NMR (two cells discharged with tetraglyme and four cells discharged with DME electrolyte solvents) experiments and tomography (two cells discharged with the tetraglyme

electrolyte solvent). When disassembling the cells, precautions were taken so that all measurements were conducted on samples that had not been exposed to air. After discharge, the cells were disassembled in a glovebox, and each cathode was put in a vial with pure DME to remove the salt and electrolyte. DME was used to wash out the salt because of its low viscosity and because it evaporates easily.

For the PFG measurements, the cathode was dried in the prechamber of the glovebox under vacuum. The dried electrode was then placed in another vial with pure tetraglyme. The vial with the tetraglyme soaked electrode was put under vacuum for 3 min to remove gases inside the pores and help with the wetting of the small pores by the solvent molecules; the electrode was left to soak in the solvent for 1 h. After that, the electrode surface was gently dried on a lab paper towel (as discussed below) and the electrode was put into a sealed plastic bag (Figure S1).

For the tomography experiments, the electrodes were transferred after washing with DME into an argon filled glove bag with an optical microscope for further sample preparation. The electrodes were chopped into small pieces. Thereafter beneath the microscope, one was selected, with the aid of a microcontroller and epoxy, a piece that fills the field of view (55  $\mu\text{m}$ ) of the transmission X ray microscope. The mounted sample was inserted with care into a Kapton tubing and sealed by Torr Seal curing at 50 °C overnight to avoid humidity contamination of the  $\text{Li}_2\text{O}_2$  particles.

**PFG-NMR Experiments. Pulse Sequence and Theory.** For diffusion NMR studies, the position of a nucleus is typically encoded by applying a linear magnetic field gradient along the magnetic field axis,  $\Delta B(g_z) = g_z z$ , superimposed on the static homogeneous magnetic field  $B_0$ . In this work, the so called Stimulated Echo (STE) pulse sequence  $90^\circ \tau - 90^\circ \tau' 90^\circ \tau -$  acquisition combined with magnetic field gradient pulses (Figure 2) was employed. The STE pulse sequence works

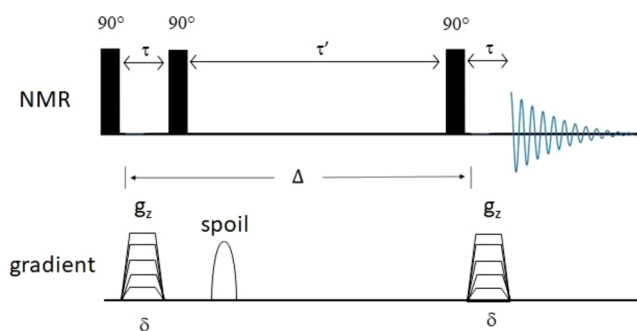


**Figure 2.** Pulse sequence used for the stimulated echo pulsed field gradient NMR experiments: (top) NMR frequency pulses and (bottom) gradient pulses.

well for NMR nuclei with transversal relaxation times shorter than spin–lattice relaxation times, as is typically the case for molecules with slow or restricted mobility.

For a linear magnetic field gradient  $g_z$  along the magnetic field axis, the total magnetic field experienced by the observed NMR nuclei is

$$B(z) = B_0 + g_z z \quad (1)$$

After the initial  $90^\circ$  radio frequency (rf) pulse, a magnetic field gradient pulse of duration  $\delta$  is applied to encode the NMR coherences with the locations of the molecules in the system.

The second  $90^\circ$  pulse at time  $\tau$  stores this encoded coherence along the magnetic field axis. Then, the molecules are given a certain time  $\tau'$  to diffuse before the final  $90^\circ$  pulse followed by another gradient pulse (equal to the first) is applied to decode the location tags. The three rf pulses combined with the gradient pulses produce a stimulated echo signal at time  $t$  after the last pulse.

The idea behind this pulse sequence is that if molecules do not move at all during  $\Delta$  (the diffusion time between the two gradient pulses, approx.  $\tau + \tau'$ , Figure 2), the encoding and decoding magnetic fields will be the same and the echo intensity of the (stimulated) echo signal for these molecules will be maximal. By contrast, if molecules diffuse during the pulse sequence, then they will experience different magnetic encoding and decoding fields. Consequently, the intensity of the echo signal will decrease. An effective diffusion coefficient ( $D_{\text{eff}}$ ) can be determined by applying a range of gradients for a fixed value of  $\Delta$  and subsequently fitting the signal intensity  $I'$  as a function of gradient strength  $g_z$  to the Stejskal–Tanner equation (see Figure S2).<sup>41</sup> For the PFG stimulated echo experiment with the pulse sequence depicted in Figure 2, the equation is

$$I' = I'_0 \exp \left[ -D_{\text{eff}} \gamma^2 g_z^2 \delta^2 \left( \Delta - \frac{\delta}{3} \right) \right] \quad (2)$$

where  $\gamma$  is the gyromagnetic ratio of the observed NMR nuclei, typically  $^1\text{H}$ .<sup>41,42</sup> In practice, to avoid gradient ringing effects, trapezoid shaped gradient pulses were used. Any remaining coherence not stored along the magnetic field axis by the second  $90^\circ$  pulse was suppressed by the spoil pulse.

For the pure tetraglyme measurement (bulk diffusion), the diffusion time  $\Delta$  selected in the PFG NMR experiment does not affect the diffusion coefficient as the diffusing molecules are not restricted in their motion. For the diffusion in porous media, the diffusion time plays an important role. If the diffusion time is too short, then, the diffusing molecules will not encounter any pore walls, and the calculated diffusion coefficient will be similar to the bulk diffusion coefficient. When increasing  $\Delta$ , the mobile molecules will diffuse further and collide with pore walls (Figure 3a). Hence, the effective

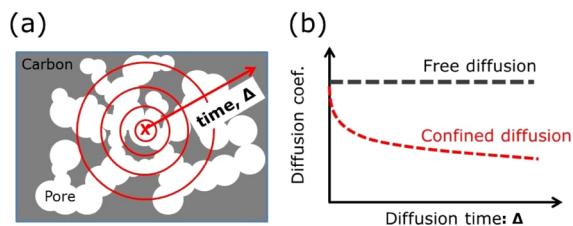


**Figure 3.** (a) Illustration of the area covered by a diffusing molecule with time. (b) Schematic representation of free diffusion and confined diffusion as a function of diffusion time.

diffusion coefficient will decrease (Figure 3b). For sufficiently large diffusion times, the confined diffusion coefficient converges to a value corresponding to long range diffusion, which is the one suitable for extracting the tortuosity factor. The NMR technique used here is not spatially resolved, and in a Li  $\text{O}_2$  battery, the discharge products can have non uniform distribution along the electrode thickness due to slow oxygen transport. A low discharge current density has been used to minimize this effect.

**Relation between the Tortuosity Factor and Diffusion Coefficients.** The porosity of an electrode is the fraction of the void (pore) volume in the total electrode volume. The tortuosity factor is a measure of the geometric complexity of a porous medium, and it is usually defined as the squared ratio between the curved paths followed by a fluid in the porous medium over a straight path. The porosity and tortuosity factor both affect the effective diffusion coefficient in a porous electrode. When there is a more porous volume (high porosity), then, the diffusion is less restricted, so the porosity and effective diffusion coefficients are positively correlated with each other. When the tortuosity factor increases, the diffusion paths of the mobile species are more curved, and their effective diffusion coefficients decrease. Hence, the tortuosity factor and effective diffusion coefficients are anticorrelated. Following these intuitive considerations, the tortuosity factor ( $\tau$ ) is defined with respect to the effective diffusion coefficient ( $D_{\text{eff}}$ ), the bulk diffusion coefficient ( $D_0$ ) and the porosity ( $\epsilon$ ) as<sup>43</sup>

$$D_{\text{eff}} = \frac{\epsilon}{\tau} D_0 \quad (3)$$

By knowing  $D_0$  and  $D_{\text{eff}}$  one can calculate  $\frac{\epsilon}{\tau}$ .

In this work, the porosity and tortuosity factor are considered to be a reflection of the structural properties of the carbon cathode. That is, they mainly depend on the porous medium and its mesostructure and not on the nature of the diffusing species, implying that the diffusing species do not bind to the carbon mesostructure, or that the nature of the interaction does not vary between different solvents. Different molecules or ions will not necessarily experience the same porosity and tortuosity factor in a given medium. For example, if molecule B is twice as big as molecule A, some parts of the porous electrode might not be accessible to B due to its size, and as a result, a smaller effective porosity and larger tortuosity factor will be determined when using B as a probe. The porosity and tortuosity factor might also depend on the rigidity/flexibility of molecules A and B. In practice, however, the size differences between relatively similar molecules, e.g. the different solvents used in Li  $\text{O}_2$  batteries electrolytes, are limited, and for the purpose of the current work, it is possible to assume that the porosity and tortuosity factor measured with these molecules reflect conditions experienced by typical battery electrolytes inside the carbon structure. The measurements require a molecule with the appropriate diffusion coefficient and relaxation time to sample the different pores and move a sufficient distance within the timescale of the PFG NMR experiment; here, the motion of  $^1\text{H}$  nuclei in the tetraglyme solvent was tracked by NMR. It is worth noting that oxygen molecules cannot be probed directly using  $^{17}\text{O}$  NMR due to the paramagnetic character of  $\text{O}_2$  and the low natural abundance of  $^{17}\text{O}$ . As the oxygen molecules are dissolved in the electrolyte, we assume that the effect of confinement on these molecules will be similar to the one on the solvent molecules.

**Experimental Details.** A 300 MHz Avance III Bruker NMR spectrometer equipped with a gradient amplifier, Diff50 gradient stack, and a 10 mm  $^1\text{H}$  coil configuration was used for the  $^1\text{H}$  PFG NMR experiments.  $90^\circ$  pulses of  $14.7 \mu\text{s}$ , a (half height) gradient duration  $\delta$  of 1 ms, and a time  $\tau$  between the first two pulses of 1.5 ms were employed. The overall diffusion time  $\Delta \approx \tau + \tau'$  was varied between 10 and 1200 ms. The gradient amplitude  $g_z$  was varied between 0 and 200  $\text{G cm}^{-1}$  (calibrated versus the self diffusion coefficient of neat

water,  $2.20 \times 10^{-9} \text{ m}^2 \text{ s}^{-1}$ , at  $25^\circ\text{C}$ ). The STE was recorded in the time domain for 16 different gradient values. PFG NMR measurements were conducted as described above with a varying diffusion time. For the long range effective diffusion coefficients, the PFG NMR measurements with diffusion time 1200 ms are used. The NMR experiments are carried out at  $25^\circ\text{C}$  with temperature controlled with water flow.

The STE signals were then transformed into the frequency domain, the resulting NMR peaks integrated, and the peak integrals plotted as a function of the gradient value. NMR data processing is done within the Bruker NMR software Topspin to extract intensities. Further analysis and fitting of intensities to the Stejskal–Tanner equation are done with MATLAB software.

**Tomographic Imaging.** An X ray nano tomography experiment with 54 nm spatial resolution (voxel size 54 nm) was done using 50 nm outermost zone width Fresnel zone plate optics and was performed in 32 ID C in the advanced photon source (APS) synchrotron at Argonne National Laboratory.<sup>44</sup> A Beam Shaping Condenser of a 60 nm outermost zone width was used. The in line Zernike phase contrast technique involving a phase ring in the back focal plane of the zone plate was used to increase the contrast between carbon and lithium peroxide.<sup>45</sup> Measurements were performed at 8 keV with a monochromatic beam ( $\Delta E/E = 10^{-4}$ ). The distance sample to detector of 3329 mm provided an X ray magnification of 46. Projections of 721 were acquired within  $180^\circ$  ( $0.25^\circ/\text{frame}$  and 1 second per frame) rotation with a FLIR GS3 U3 51S5M C detector. Projections were preprocessed with packages present in Tomopy<sup>46</sup> and then reconstructed into volumes by the GPU accelerated SIRT method<sup>47</sup> (200 iterations, more iterations induce noises) in the same library. The WEKA trainable segmentation Fiji plug in Random Forrest based machine learning was used for the multiphase segmentation.<sup>48</sup> The surface, porosity, and tortuosity factor determinations are conducted respectively with in house codes developed by the authors<sup>39</sup> and Taufactor;<sup>49</sup> Taufactor calculates the tortuosity factor from the tomographic images, simulating diffusion by solving Fick's second law.<sup>49</sup>

**Pore Network Model.** To assess the effect of the discharge product growth mechanism on pore clogging, a pore network model already described in previous publications was used.<sup>39,40</sup> The galvanostatic discharge potential profiles (the discharge current density is  $100 \mu\text{A g}^{-1}$ ) for a Super P pristine electrode mesostructure obtained via tomographic imaging were simulated.<sup>39</sup> A tomographic image of the pristine Super P electrode from our previous work<sup>39</sup> was used as we do not have the tomographic image for the pristine electrode used in this work. As the tomographic image in our previous work and the current study use the same Super P material from the same supplier, their microstructure should have a similar morphology. A system size of  $4 \times 4 \times 5 \mu\text{m}$ , along two radial and the electrode thickness directions, respectively, was used. In the model, an overall electrochemical reaction is considered where two lithium ions react with an  $\text{O}_2$  molecule to form  $\text{Li}_2\text{O}_2$ . Five simulations were completed on the same starting electrode mesostructure with five different escape factors ( $\chi = 0, 0.25, 0.5, 0.75,$  and  $1$ ) to study the effect of the discharge particle growth mechanism on the pore clogging and tortuosity factor evolution. The escape factor represents the propensity of  $\text{LiO}_2$  intermediate molecules of the discharge process to dissolve in the electrolyte and contribute to the growth of large discharge

particles. By increasing the escape factor from 0 to 1, we move from a thin film growth to a solution phase growth mechanism (and the formation of large particles).

**Kinetic Monte Carlo Model.** To study the effect of pore size and the importance of the Knudsen diffusion effect in the systems explored here, we developed a kinetic Monte Carlo model. The Knudsen effect describes the diffusion in narrow pores where the diffusion coefficient is affected by collisions of the mobile species with the pore wall. While intuitively, smaller pores will lead to more collisions and slower diffusion, a model was constructed to obtain quantitative information on this effect for the pore sizes relevant to this study. The kMC model is adapted from a previously published model, which had been used to simulate the discharge process in  $\text{Li O}_2$  batteries.<sup>50</sup>

A cylindrical pore geometry (Figure 4) was used to simulate diffusion in a pore. The pore volume was sliced into voxels

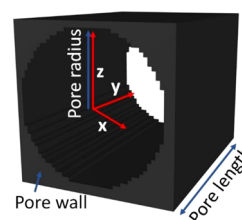


Figure 4. Cylindrical pore geometry considered in the kMC model.

with a side length of 0.5 nm, which is assumed to be the hydrodynamic size of a dissolved  $\text{O}_2$  molecule. The hopping frequency ( $\gamma_i$ ), also called the event frequency, was calculated as

$$\gamma_i = \frac{2D_{\text{O}_2}}{s^2} \quad (4)$$

where  $D_{\text{O}_2}$  is the bulk diffusion coefficient of  $\text{O}_2$ , and  $s$  is the voxel size. In the model, the  $\text{O}_2$  molecules can jump (or diffuse) to 18 sites (6 face sharing and 12 edge sharing) provided that those neighboring voxels are empty. Periodic boundary conditions in the direction of the pore length were used.

In this kMC model, only translational motion and no reactions were simulated. A variable step size method is used<sup>50</sup> and the time step is calculated as

$$\Delta t = \frac{-\ln(\rho_1)}{\gamma_{\text{tot}}} \quad (5)$$

$$\gamma_{\text{tot}} = \sum_{i=1}^N \gamma_i \quad (6)$$

where  $\rho_1$  is a random number in the interval  $(0,1]$ , i.e., larger than zero and smaller or equal to one,  $\gamma_{\text{tot}}$  is the sum of all event frequencies, and  $N$  is the total number of possible events.

The event occurring at a given step is chosen according to the weighted probability of each event. The event  $j$  is selected according to the following rule

$$\sum_{i=1}^j \gamma_i < \rho_2 \gamma_{\text{tot}} \leq \sum_{i=1}^{j+1} \gamma_i \quad (7)$$

where  $\rho_2$  is a random number in the interval  $(0,1]$ . This process allows for the simulation of a system with various event

frequencies, including a mixture of fast and slow events. In the present case, only events related to the transport of a single type of molecule ( $O_2$ ) are considered. However, the script is written in a general form to be able to work with many event types if necessary.

It is worth noting that, in this work, an approach upgraded from the ones previously reported was used.<sup>50,51</sup> A simplified scheme of our algorithm is given in Figure S3. In this new scheme, all possible events at the beginning of the calculation are determined and then stored in an easy to update data structure. In the main loop, only the events, which are in the vicinity of the executed events, are updated. The number of events updated at each timestep is around 18 against several thousands when the full ensemble of possible events is scanned. As a consequence, this procedure is much more efficient, and calculations are much faster: the new procedure is about 2000 times faster than the previously reported ones<sup>50,51</sup> for the system under investigation here.

To extract the diffusion coefficients from the particles trajectories, the mean square displacement (MSD) method was used where the MSD function is defined as

$$\text{MSD} = \langle |d_{i,t} - d_{i,t_0}|^2 \rangle \quad (8)$$

where  $d_{i,t}$  is the position of molecule  $i$  at time  $t$  and  $d_{i,t_0}$  is the position of the same molecule at time  $t = 0$ . The  $\langle \dots \rangle$  sign corresponds to an average over all  $O_2$  molecules. After a long enough simulation time, the MSD curve becomes linear (Figure 5), and the diffusion coefficient ( $D$ ) can be retrieved from its slope according to Einstein relation

$$D = \frac{\text{MSD}}{6t} \quad (9)$$

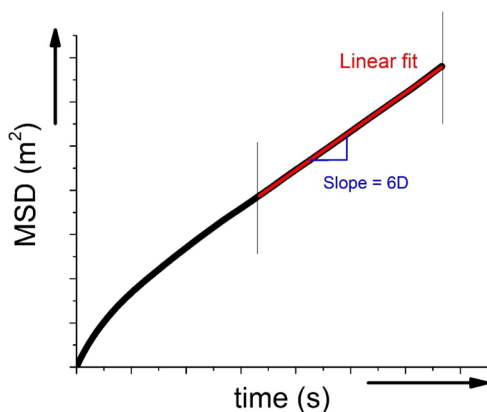


**Figure 5.** Illustration of the determination of a diffusion coefficient from an MSD curve. Two vertical lines show the time interval where the MSD curve is linear with time. The red line is the fit to the MSD curve in the selected region.

For kMC simulations with different cylinder diameters, if the cylinder length was kept the same for all pore sizes, there would be a very significant variation in the number of oxygen molecules in the pores as cylinders with large diameters would contain many more molecules than cylinders with smaller diameters. This would affect the MSD fitting accuracies. To have the same amount of oxygen molecules in all the calculations, the porous volume is kept constant and equal to  $783,398 \text{ nm}^3$  (i.e.,  $6,267,184$  voxels), which corresponds to the pore volume of a cylinder with a diameter of 100 nm and a

length of 100 nm. This means that cylinders with smaller pore diameters will have larger pore lengths. The amount of oxygen in each calculation is set to 1256 molecules. The total simulation time is  $2 \mu\text{s}$ .

## RESULTS AND DISCUSSION

**Measurement of Bulk Diffusion Coefficients and Evaluation of Drying Procedures.** The bulk diffusion coefficient in the pure tetraglyme solvent (i.e., the value measured under nonconfined conditions) was first measured via  $^1\text{H}$  PFG NMR spectroscopy and determined to be  $3.420 \times 10^{-10} \text{ m}^2 \text{ s}^{-1}$ , with a 95% confidence range of  $\pm 0.005 \times 10^{-10} \text{ m}^2 \text{ s}^{-1}$  (i.e., a 0.14% error bar; see Figure S2 for details). To measure the diffusion of tetraglyme confined in the porous structure of a Super P electrode, it is important that all the solvent molecules are inside the porous structure and that there are no molecules on the surface of the electrode since the latter will have larger effective diffusion coefficients than the confined ones and will affect the average measured diffusion coefficient. Two different drying approaches were tested. For the first one (the *gently dried* method), the soaked electrode is gently touched and wiped on both sides using a lab paper towel. For the second drying approach (termed *thoroughly dried*), the *gently dried* electrode is put on a lab paper towel and another piece of paper towel is put on top of it. Then, a slight pressure was applied by hand to soak away any remaining liquid on the surface.  $^1\text{H}$  NMR spectra were acquired from samples prepared via the three approaches and used to estimate the relative solvent quantities (Figure S4) and show that the free electrolyte (sharp) signal was removed even after gently drying. Thoroughly drying removed further a 45% of the total solvent. Diffusion coefficient measurements on electrodes dried with the two techniques were then compared with results from two other samples: bulk tetraglyme; an electrode flooded with an excess of the tetraglyme solvent and is shown in Figure 6.

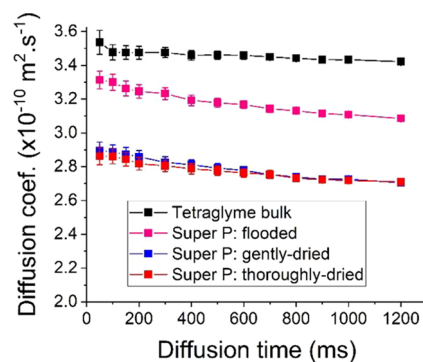


**Figure 6.** Diffusion coefficients for bulk tetraglyme and tetraglyme in three Super P electrodes, determined with PFG methods as a function of diffusion time,  $\Delta$ .

Unlike the neat tetraglyme, for samples containing the porous electrode, the effective diffusion coefficient decreases as the diffusion time increases, which is a signature of confined diffusion (Figure 3). The similar diffusion coefficients obtained for the *gently dried* and *thoroughly dried* samples provide confidence that both approaches are sufficient to remove the excess liquid from the surface of the electrodes, consistently with the  $^1\text{H}$  NMR spectra of the solvents (Figure S4). If that was not the case, the diffusion coefficients for the *gently dried*

case would be higher than the *thoroughly dried* case as demonstrated by the results for the flooded sample. Even though a significant amount of additional electrolytes was removed (45%) in the *thoroughly dried* sample (vs the *gently dried* sample), this did not result in any visible effects from restricted diffusion due to empty pores with no solvent, as the diffusion coefficients measured at longer diffusion times for the *gently dried* and *thoroughly dried* were essentially identical. For subsequent experiments, the *gently dried* approach was used.

**Tortuosity Factor Evolution along Discharge.** *NMR.* To study the tortuosity factor evolution along the depth of discharge, several self standing Super P electrodes were discharged at a discharge current of 50  $\mu\text{A}$ . For the tetraglyme solvent, two electrodes are discharged: one cell is discharged to the end of capacity and the other is stopped halfway when a 253 mAh  $\text{g}^{-1}$  capacity is reached (Figure 7a). As there is some

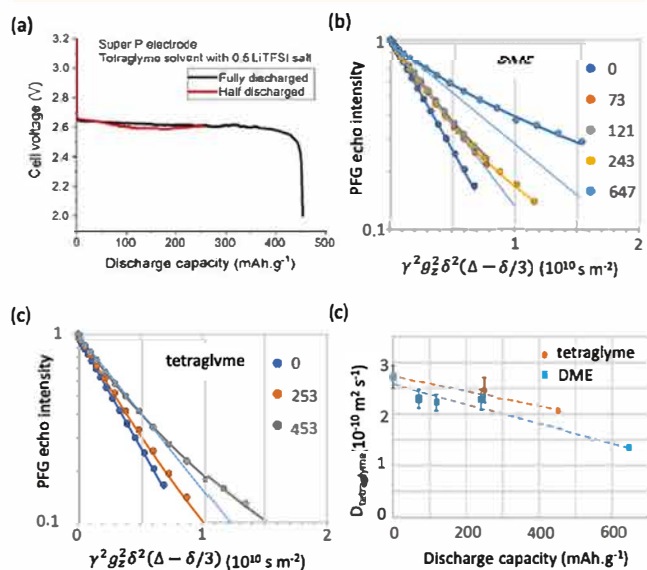


**Figure 7.** Tetraglyme diffusion in self standing Super P electrodes as a probe for pore clogging at various states of discharge against lithium. (a) Constant 50  $\mu\text{A}$  current discharge profiles of Super P with 0.5 M LiTFSI tetraglyme as electrolyte. (b, c) Diffusion NMR of Super P electrodes discharged in (b) DME and (c) tetraglyme.  $^1\text{H}$  PFG NMR echo decays vs the composed experimental parameter  $\gamma^2 g_z^2 \delta^2 (\Delta - \delta/3)$  (eq 2) (eq 2) increasingly deviate from monoexponential behavior (dashed lines) at increasing depth of discharge. The data are well described in terms of a biexponential model (solid lines) with two discharge constant diffusion coefficients and fractions, which vary with discharge. Phenomenologically, the two fractions represent the clog free and clogged electrode parts. (d) Effective tetraglyme diffusion coefficients (a weighted average of the two diffusion coefficients) in self standing Super P electrodes discharged with either DME or tetraglyme as electrolytes as a function of discharge. Dashed lines are a guide to the eye. The PFG NMR data shown here have been recorded for a diffusion time  $\Delta = 1200$  ms. For PFG echo decays at different  $\Delta$  times, see Figure S5.

variability in the discharge capacity of Li  $\text{O}_2$  batteries, the definition of “halfway” is only an approximation.<sup>39,52</sup> For the DME solvent, four electrodes are discharged, and the discharge processes are stopped at 73, 121, 243, and 647 mAh  $\text{g}^{-1}$ , the last one being the end of discharge.

All electrodes, whether discharged with tetraglyme or DME electrolyte, were dried and saturated with pure tetraglyme (without LiTFSI). Then, pore clogging was probed by

measuring solvent diffusion at varied diffusion times in the range 20–1200 ms (Figure S5) using PFG NMR. Here, we focus on the data obtained with the longest diffusion time,  $\Delta = 1200$  ms where diffusion coefficients in pristine electrodes approach a convergence limit (Figure 6). The root mean square displacement  $\langle r^2 \rangle^{1/2}$  of bulk tetraglyme molecules indicates that electrolyte molecules travel approximately 50  $\mu\text{m}$  in this time ( $\langle r^2 \rangle^{1/2} = (6 \cdot D \cdot t)^{1/2} = (6 \cdot D \cdot \Delta)^{1/2} = (6 \cdot 3.42 \cdot 10^{-10} \text{ m}^2 \text{ s}^{-1} \cdot 1.2 \text{ s})^{1/2} = 49.6 \mu\text{m}$ ). This ensures that the diffusion coefficients do not measure local (*i.e.*, short range) motions but correspond to long range diffusion.

Figure 7b,c and Figure S5 show PFG echo intensities versus the composite experimental variable  $X = \gamma^2 g_z^2 \delta^2 (\Delta - \delta/3)$  ( $\gamma$ ,  $g_z$ ,  $\delta$ , and  $\Delta$  defined in eq 2). The observed decays for discharged electrodes deviate significantly from single component behavior (eq 2) and increasingly so as the depth of discharge increases. The fast decay components reflect relatively unrestricted solvent diffusion, whereas the slow decay components represent the confined diffusion in clogged parts of the porous electrode. This heterogeneity also arises because of the geometry of the lithium oxygen battery, oxygen entering from one side of the electrode and  $\text{Li}^+$  ions from the other. All PFG curves for tetraglyme diffusion in the electrodes at varied diffusion times and different stages of discharge in DME or tetraglyme are well described by a biexponential function  $f_A \exp(-D_A X) + f_B \exp(-D_B X)$ . To improve the consistency of the analysis, all curves obtained for the same diffusion time, but at different states of discharge, are fit in a combined manner. The specific fit procedure treats the two diffusion coefficients as independent of the discharge stage and allows the components amplitudes to vary freely. While it is a simplification to divide the pores into two categories, clog free and clogged with fast and slow diffusion, respectively, the model works well in a phenomenological way and can be used to explore distributions in diffusion coefficients.

Pairs of tetraglyme diffusion coefficients ( $D_A$ ,  $D_B$ ) extracted for electrodes discharged in DME and tetraglyme, as a function of diffusion time are plotted in Figure 8. The coefficient  $D_A$  of

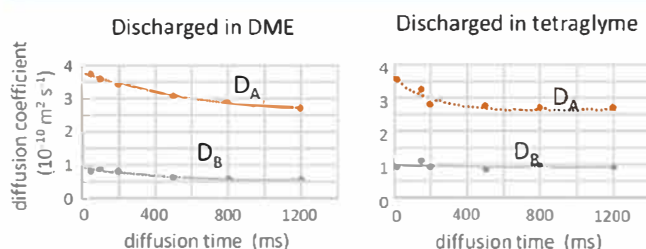


**Figure 8.** Diffusion coefficients pairs ( $D_A$ ,  $D_B$ ) extracted from bicomponent fits to PFG decays as a function of the diffusion time for an electrode discharged in DME (left) and tetraglyme (right). The biexponential model assumes that the values of the diffusion coefficients do not change with the discharge stage, but the relative fraction of each component does. Changes in pore clogging are reflected by the fraction of each component (Table 1).

the mobile component decreases in both electrodes from close to the free tetraglyme diffusion value  $3.5 \cdot 10^{-10} \text{ m}^2 \text{ s}^{-1}$  at short diffusion times toward  $2.5 \cdot 10^{-10} \text{ m}^2 \text{ s}^{-1}$ . This decrease likely indicates that even the mobile component in the largely unclogged pores experiences diffusion restrictions at sufficiently long diffusion times. The  $D_A$  decrease also reflects the continuous solvent exchange between clog free and clogged



**Table 1.** Fraction  $f_B$  of Immobile/Restricted Diffusion Component as a Function of Depth of Discharge and of the Diffusion Time, Tentatively Representing the Fraction of Clogged Pore Space

time	discharged in DME					discharged in tetraglyme		
	0 mA h g <sup>-1</sup>	73 mA h g <sup>-1</sup>	121 mA h g <sup>-1</sup>	243 mA h g <sup>-1</sup>	647 mA h g <sup>-1</sup>	0 mA h g <sup>-1</sup>	253 mA h g <sup>-1</sup>	454 mA h g <sup>-1</sup>
20 ms						0.16	0.36	0.32
50 ms	0.19	0.16	0.35	0.22	0.35			
100 ms	0.17	0.19	0.36	0.25	0.45			
150 ms						0.13	0.30	0.34
200 ms	0.19	0.18	0.32	0.24	0.53	0.00	0.20	0.24
500 ms	0.07	0.17	0.26	0.21	0.54	0.00	0.13	0.26
800 ms	0.04	0.14	0.24	0.21	0.60	0.00	0.15	0.33
1200 ms	0.00	0.19	0.22	0.20	0.65	0.00	0.13	0.36

parts of the porous network within the timeframe of the measurement (0–1200 ms). The second coefficient  $D_B$  decays from ca.  $1 \times 10^{-10}$  to  $0.51 \times 10^{-10} \text{ m}^2 \text{ s}^{-1}$  in the DME discharged electrode but is fairly constant around  $1 \times 10^{-10} \text{ m}^2 \text{ s}^{-1}$  in the tetraglyme discharged electrodes.

With the values of the diffusion coefficient pair ( $D_A$ ,  $D_B$ ) assumed independent of the discharge stage, the degree of pore clogging at varied discharge is reflected by the fraction  $f_B$  (representing the volume fraction of clogged pore) of the relatively immobile or restricted diffusion coefficient (Table 1). The fraction  $f_B$  in the bicomponent model generally increases with state of discharge, as expected, while for a given diffusion time  $f_B$ , values are generally higher for the electrodes discharged in DME than in tetraglyme. Pore clogging thus appears to occur more frequently during discharge in DME. Interestingly, fraction  $f_B$  decreases with the diffusion time indicating that the diffusion appears to be more homogeneous at longer diffusion times as a larger pore volume is sampled. This may at least in part be ascribed to continuous solvent exchange between clog free and clogged parts of the porous network, an effect that becomes more pronounced as the diffusion time increases.

The tortuosity model treats the porous network as homogeneous, whereas the bicomponent model artificially divides the pore network into two categories, clog free and clogged pores. In reality, of course, various degrees of pore clogging may occur in different pores, and dynamic solvent exchange between clog free and clogged pore areas may also reduce the contrast between these regions.

A possible link between the tortuosity model and bicomponent model can be established by deriving the weighted average diffusion coefficient  $D_{av} = f_A D_A + f_B D_B$  from the bicomponent fit (Table S1). For the biexponential model used in our analysis, this corresponds to the initial slope of the decay. This represents an alternative way to characterize the PFG curves with a single effective diffusion parameter. The average diffusion coefficient  $D_A$  is always lower than the free tetraglyme diffusion coefficient and generally decreases with discharge and the overall diffusion time, as expected. The weighted average diffusion coefficient from the biexponential model for a diffusion time of 1200 ms is shown on Figure 7d and can be compared with the monocomponent fitting shown on Figure S5. The diffusion coefficients have the same trends in both cases. However, the errors in the bicomponent fitting are significantly lower (the single component fit showing errors as large as 60%, see the Supporting Information for the error analysis, and bicomponent fit leading to errors below 20%), supporting our analysis of the diffusion in terms of more than one diffusion coefficient. Our simple analysis considers two

types of diffusion in the electrode: one in more restricted (clogged pores) and the other in less restricted (clog free) porous domains. In reality, the electrode will have a distribution of diffusion domains with varying degrees of restriction (clogging).

The overall trend observed for both solvents is that the effective diffusion coefficient decreases as the cell is discharged further and the transport through the electrode becomes more tortuous. This is consistent with the growth of discharge products leading to a reduction of porosity via pore shrinkage and clogging of some pores. Higher effective diffusion coefficients are measured for the electrodes discharged in the tetraglyme based electrolyte compared to the electrodes discharged in the DME based electrolyte. This is ascribed to the larger particles formed and more pore clogging in DME: DME has a higher donor number than tetraglyme, and thus, we expect the corresponding cells to show larger  $\text{Li}_2\text{O}_2$  particles than the tetraglyme ones.<sup>22,23</sup>

The evolution of the tortuosity factor can be calculated from the effective diffusion coefficients using eq 3. The porosity of the pristine electrode is 0.81, as calculated from the measured electrode dimensions and mass (see Table S2 in the Supporting Information). For this calculation, we assume that the only discharge product is  $\text{Li}_2\text{O}_2$ , which allows the volume of  $\text{Li}_2\text{O}_2$  to be calculated from the discharge capacity and the change of porous volume, and porosity, to be estimated. The evolution of the tortuosity factor was then estimated via Bruggeman relation using eq 10

$$\tau = \frac{1}{\epsilon^{0.5}} \quad (10)$$

and compared with that obtained from the PFG data in Figure 9.

The tortuosity factor values extracted from PFG NMR measurements for DME change more drastically than suggested by the Bruggeman relation, particularly for DME.<sup>53</sup> The tortuosity factor evolution depends on the porosities of the pristine and discharged electrodes, which are only estimated here. Thus, we have also plotted  $\frac{\tau}{\epsilon}$  vs depth of discharge and is shown in Figure S6 since this does not require any assumptions concerning the change in porosity: it is simply the ratio of  $D_{\text{eff}}/D_0$  (see eq 3). The plot shows the same trends as Figure 9, supporting our analysis of tortuosity vs depth of discharge.

**Tomography.** To measure the change of tortuosity factor with a second technique, tomographic imaging was conducted on two samples: partially (206 mAh g<sup>-1</sup>) and fully (362 mAh g<sup>-1</sup>) discharged Super P electrodes with 0.5 M LiTFSI in

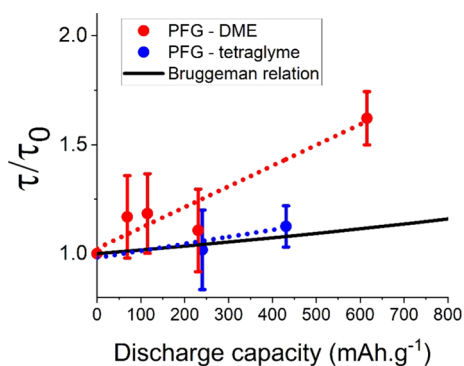


**Figure 9.** Tortuosity factors in pristine, partially, and fully discharged self standing Super P electrodes, extracted from PFG NMR measurements using weighted average diffusion coefficients from the biexponential model. The solvent used for discharge is indicated in the legend. The Bruggeman relation is applied by assuming that all discharge products are  $\text{Li}_2\text{O}_2$ . Dashed lines for experimental data are linear fit to the data points weighted with the error bars. An explanation of the error analysis is given in the Supporting Information.

tetraglyme electrolytes. Tortuosity factor values of 4.95 and 5.4 are calculated from the tomographic images for partially and fully discharged cells, respectively. To compare them with the evolution of tortuosity factor values measured by PFG NMR experiments, we compare the rate of change of the tortuosity factor, *i.e.*, the slopes of the discharge capacity versus  $\frac{\tau}{\tau_0}$  plots shown in Figure 9 (Table 2). Although the errors associated

**Table 2.** Rate of Change of the Tortuosity Factor along Discharge, Calculated with Three Different Techniques

sample and method	rate of tortuosity factor change along discharge $\times 10^{-4} \text{ (g m}^{-1}\text{A}^{-1}\text{ h}^{-1}\text{)}$	$\left(\frac{\tau}{\tau_0}\right)$ capacity
Bruggeman relation	$2.00 \pm 0.03$	
PFG-NMR tetraglyme	$7.5 \pm 2.1$	
PFG-NMR DME	$16.6 \pm 2.5$	
TXM tetraglyme	5.9	

with the PFG measurements are large, which is largely ascribed to differences between cells, each *ex situ* PFG measurement was made on a different cell, and errors in the PFG

measurements (as discussed above) associated with describing the PFG data with a single diffusion coefficient for the fully discharged sample, a significant difference is seen between the values calculated for the tetraglyme and DME discharged electrodes. The tortuosity factor value evolution calculated from tomographic images for electrodes discharged with tetraglyme electrolyte is close to the value measured by PFG NMR experiments for the same electrodes and very different from the electrodes discharged in DME based electrolyte and the Bruggeman estimation.

The analysis of the tomographic images also allows us to extract pore size distributions, which show an overall increase in the fraction of smaller pores, suggesting a shrinkage of the pores (Figure 10). However, clogging of micropores with pore sizes below 54 nm is hard to evaluate solely by tomography measurements due to imaging resolution, and any analysis should be coupled with other techniques.

**PNM Modeling.** The PNM approach<sup>39</sup> was then used to explore the hypothesis that the formation of larger discharge particles leads to more pore clogging. In the PNM approach, the escape factor parameter,  $\chi$ , can be varied to adjust the relative contributions of the film growth mechanism versus the particle growth mechanism. A larger value of  $\chi$  corresponds to a more predominant particle growth mechanism and thus the formation of larger particles of  $\text{Li}_2\text{O}_2$ .

Figure 11 shows the evolution of the number of clogged pores along discharge for five different escape factors, the

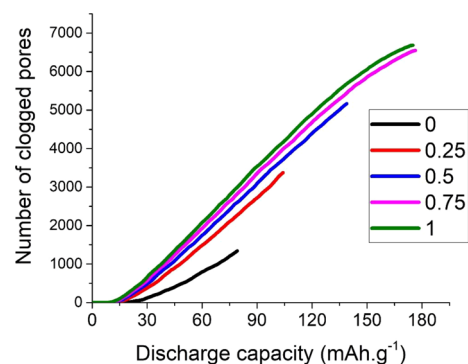


**Figure 11.** Number of clogged pores for the Super P electrode structure calculated using PNM modelling of the pristine Super P electrode structure obtained from tomographic imaging. The discharge current density is  $100 \mu\text{A g}^{-1}$ . Plots are shown for five escape factors ( $\chi = 0, 0.25, 0.5, 0.75, \text{ and } 1$ ).

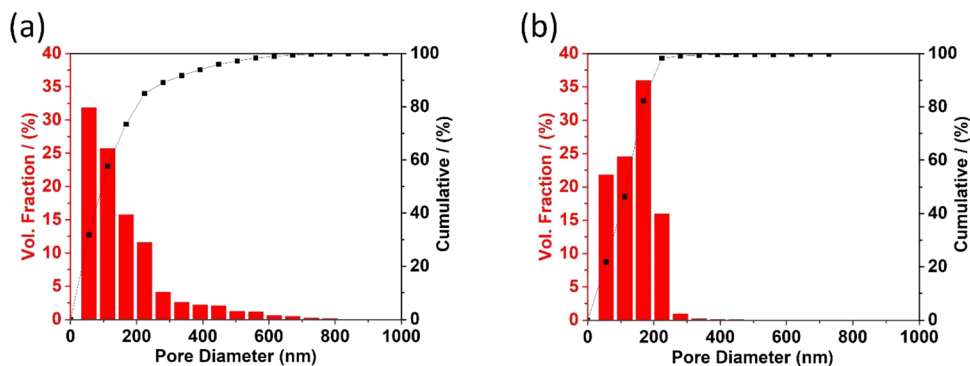


**Figure 10.** Pore size distributions obtained from tomographic images of (a) partially  $206 \text{ mAh g}^{-1}$  and (b) fully  $362 \text{ mAh g}^{-1}$  discharged Super P electrodes with  $0.5 \text{ M LiTFSI}$ , tetraglyme electrolytes at  $50 \mu\text{A}$  discharge current.

number of clogged pores being higher for larger escape factors. This calculation thus provides a plausible interpretation as to why the effective diffusion coefficients for electrodes discharged in DME based electrolytes decreases faster along discharge. It is worth noting that there is a large difference between the curves for  $\chi = 0$  and  $\chi = 0.25$  but the changes are more limited for higher escape factors. This would indicate that even without being predominant, the onset of particle growth is enough to significantly enhance the pore clogging phenomenon. Indeed, as shown in Figure S7 (the gradient in discharge products is shown in Figure S8), already for  $\chi = 0.25$ , a large number of particles of 25  $\mu\text{m}$  or larger are produced; these particles are sufficiently large to clog the majority of the pristine Super P carbon pores with a size between 25 and 50  $\mu\text{m}$ . As a consequence, the larger particles produced at higher  $\chi$  values result in less dramatic changes.

As was shown in a previous work,<sup>40</sup> PNM calculations on three dimensional electrode structures also yield larger tortuosity factor changes on discharge compared to the Bruggeman relation. The larger increase in the tortuosity factor for PNM calculations is due to the incorporation of pore clogging effects in the simulations of 3D electrode structures. Similarly here, pore clogging could be the reason why a more dramatic tortuosity factor change is observed in PFG NMR measurements compared to the Bruggeman relation.

**kMC Modeling.** Another factor that can affect the effective diffusion coefficient of a molecule in a porous media is the frequent collisions of particles with the pore wall. This phenomenon, which is called Knudsen diffusion, is particularly important when the pore is very small. This effect is naturally present in the effective diffusion coefficient measurements done with PFG NMR experiments. Yet in most cases, the tortuosity factor is considered only as a function of porosity. Here, to quantify the effect of pore size on diffusion, a kMC model is used.

To assess the importance of this effect, the bulk diffusion coefficient was given as an input and set to  $5 \cdot 10^{-9} \text{ m}^2 \text{ s}^{-1}$ , which is within the typical range of oxygen diffusion coefficients reported for Li O<sub>2</sub> battery electrolytes.<sup>22</sup> Oxygen diffusion is studied first before changing the diffusing molecule to tetraglyme molecules. Nine different pore sizes were tested, corresponding to cylindrical pores with diameters of 1, 2, 3, 4, 5, 10, 25, 50, and 100 nm, which are within the range of Super P pore sizes.<sup>8</sup> The obtained MSD curves are shown in Figure 12 (and Figure S9 for  $x$ ,  $y$ , and  $z$  contributions to the overall diffusion). The MSD values increase nonlinearly with time for short times but become linear after 1  $\mu\text{s}$ . This is particularly visible for the 100 and 50 nm pore sizes.

The diffusion coefficient as a function of the pore diameter calculated from kMC trajectories is shown in Figure 13. While the effective diffusion coefficient does not vary much for pores with diameters larger than 25 nm, a pore size effect is seen below 25 nm. The effective diffusion coefficient decreases sharply for pores with diameters below 4–5 nm.

The sensitivity of these trends on the input diffusion coefficient value and voxel size was analyzed. As the molecule tracked in the PFG NMR experiments is tetraglyme, two similar kMC calculations were done with tetraglyme as the diffusing molecule instead of O<sub>2</sub>. For the first of these two additional kMC calculations, the input value for the bulk diffusion coefficient was simply changed from the value of O<sub>2</sub> to the tetraglyme bulk diffusion coefficient (measured by PFG NMR and equal to  $3.42 \cdot 10^{-10} \text{ m}^2 \text{ s}^{-1}$ ). In the second

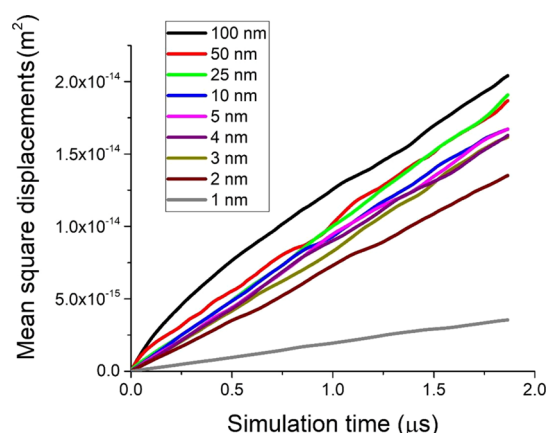


Figure 12. MSD plots obtained from kMC calculations for several pore sizes.

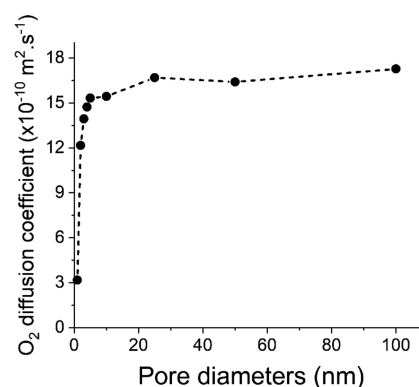


Figure 13. O<sub>2</sub> diffusion coefficients calculated using the kMC model for various pore diameters.

calculation the voxel size was changed from 0.5 to 0.75 nm (to represent the longer chain of tetraglyme molecules). The diffusion coefficient value does not change the pore size effect on the effective diffusion coefficient values, while the voxel size seems to affect the effective diffusion coefficient values only slightly (Figure S10).

These three kMC calculations confirm that the pore size effect on the effective diffusion coefficient is not noticeable for pores larger than 5 nm and only significant below that size. These trends are consistent with PFG NMR measurements conducted by Forse *et al.*<sup>35</sup> for self diffusion coefficients of ions in activated carbons for supercapacitors. They measured effective diffusion coefficients about two orders of magnitude lower for ions in nanopores compared to the bulk values. These kMC calculations and prior reports on the pore size effect on the effective diffusion coefficient confirm our assumption that the change in the measured effective diffusion coefficient values are mainly influenced by pore clogging in the electrode mesostructure.

## SUMMARY AND CONCLUSIONS

In this study, several Super P electrodes were discharged to various depths of discharge and effective diffusion coefficients of tetraglyme molecules in the porous cathodes were measured using PFG NMR experiments. This allowed for the extraction of the tortuosity factor evolution along discharge for Li O<sub>2</sub> batteries. It was shown that the tortuosity factor increases with the depth of discharge. The effect of the solvent on the

tortuosity factor evolution of Super P electrodes was also studied. When a DME based electrolyte is used, the tortuosity factor increases more dramatically than when tetraglyme is used as the electrolyte solvent. The tortuosity factor evolution along discharge is confirmed with tomographic imaging for cells discharged with tetraglyme electrolytes. This difference between solvents is attributed to the difference in the size of discharge products in the two electrolytes.

PNM and kMC calculations were used to investigate the relative importance of pore clogging and pore shrinking on the effective diffusion coefficients. PNM calculations showed that electrolytes with larger escape factor (higher donor number) lead to more pore clogging. This provides a plausible reason for why the tortuosity factor of the electrodes discharged in DME based electrolyte increases more than seen in tetraglyme. The kMC calculations show that there is indeed a pore size effect on diffusion, but it manifests itself only for very small pores with diameters below 5 nm. In Super P electrodes, less than 0.1% of the porous volume correspond to pores with radiuses below 90 nm, which makes this effect negligible in these electrodes.<sup>12</sup> In the future, these results could be integrated in the PNM model to improve its accuracy by including the pore size effect on diffusion; the PNM would capture in a better way the influence of the pore shrinkage along discharge.

These experimental and modeling results can be used to suggest ways of optimizing battery performance. For instance, using an electrolyte that promotes formation of large discharge products can provide high discharge capacities but may not perform well at high discharge rates as the pore clogging will hinder ionic transport. On the contrary, electrolytes in which small particles are favored reduce pore clogging and favor faster transport. Porous carbon materials and electrolytes thus have to be optimized in parallel to have particle sizes large enough for a high capacity but without clogging the electrode pores. The measured rate of change of tortuosity could in future work be used to optimize cell performance. For instance, there are several factors, such as high discharge current, that could lead to smaller Li<sub>2</sub>O<sub>2</sub> particle sizes. The ability to measure the electrode tortuosity after the cells have been discharged allows one to optimize the discharge rate to maximize capacity while still maintaining a low tortuosity. Furthermore, it is potentially possible to determine whether shut down of the cell is more likely due to a decrease in the overall tortuosity or to pore blockage on the air side of the electrode.

## ■ ASSOCIATED CONTENT

### ● Supporting Information

The Supporting Information is available free of charge at <https://pubs.acs.org/doi/10.1021/acs.jpcc.0c10417>.

More details on PFG NMR measurements, error analyses, calculating diffusion coefficients from kMC, and sensitivity analysis for kMC data are provided (PDF)

## ■ AUTHOR INFORMATION

### Corresponding Author

Clare P. Grey – *Department of Chemistry, University of Cambridge, Cambridge CB2 1EW, U.K.; ALISTORE European Research Institute, FR CNRS 3104, Hub de*

*l'Energie, Amiens 80039, France; [orcid.org/0000-0001-5572-192X](https://orcid.org/0000-0001-5572-192X); Email: [cpg27@cam.ac.uk](mailto:cpg27@cam.ac.uk)*

## Authors

Amangeldi Torayev – *Laboratoire de Réactivité et Chimie des Solides (LRCS), UMR CNRS 7314, Université de Picardie Jules Verne, Hub de l'Energie, Amiens 80039, France; Department of Chemistry, University of Cambridge, Cambridge CB2 1EW, U.K.; ALISTORE European Research Institute, FR CNRS 3104, Hub de l'Energie, Amiens 80039, France*

Simon Engelke – *Department of Chemistry and Cambridge Graphene Centre, University of Cambridge, Cambridge CB2 1EW, U.K.*

Zeliang Su – *Laboratoire de Réactivité et Chimie des Solides (LRCS), UMR CNRS 7314, Université de Picardie Jules Verne, Hub de l'Energie, Amiens 80039, France; Réseau sur le Stockage Electrochimique de l'Energie (RS2E), FR CNRS 3459, Hub de l'Energie, Amiens 80039, France; [orcid.org/0000-0001-7142-8977](https://orcid.org/0000-0001-7142-8977)*

Lauren E. Marbella – *Department of Chemistry, University of Cambridge, Cambridge CB2 1EW, U.K.; Department of Chemical Engineering, Columbia University, New York 10027, United States; [orcid.org/0000-0003-1639-3913](https://orcid.org/0000-0003-1639-3913)*

Vincent De Andrade – *X Ray Science Division, Advanced Photon Source, Argonne National Laboratory, Lemont 60439, United States*

Amaud Demortière – *Laboratoire de Réactivité et Chimie des Solides (LRCS), UMR CNRS 7314, Université de Picardie Jules Verne, Hub de l'Energie, Amiens 80039, France; ALISTORE European Research Institute, FR CNRS 3104, Hub de l'Energie, Amiens 80039, France; Réseau sur le Stockage Electrochimique de l'Energie (RS2E), FR CNRS 3459, Hub de l'Energie, Amiens 80039, France; [orcid.org/0000-0002-4706-4592](https://orcid.org/0000-0002-4706-4592)*

Pieter C. M. M. Magusin – *Department of Chemistry, University of Cambridge, Cambridge CB2 1EW, U.K.; ALISTORE European Research Institute, FR CNRS 3104, Hub de l'Energie, Amiens 80039, France; [orcid.org/0000-0003-1167-3764](https://orcid.org/0000-0003-1167-3764)*

Céline Merlet – *ALISTORE European Research Institute, FR CNRS 3104, Hub de l'Energie, Amiens 80039, France; Réseau sur le Stockage Electrochimique de l'Energie (RS2E), FR CNRS 3459, Hub de l'Energie, Amiens 80039, France; CIRIMAT, Université de Toulouse, CNRS, Bât. CIRIMAT, Toulouse 31062, France; [orcid.org/0000-0003-3758-273X](https://orcid.org/0000-0003-3758-273X)*

Alejandro A. Franco – *Laboratoire de Réactivité et Chimie des Solides (LRCS), UMR CNRS 7314, Université de Picardie Jules Verne, Hub de l'Energie, Amiens 80039, France; ALISTORE European Research Institute, FR CNRS 3104, Hub de l'Energie, Amiens 80039, France; Réseau sur le Stockage Electrochimique de l'Energie (RS2E), FR CNRS 3459, Hub de l'Energie, Amiens 80039, France; Institut Universitaire de France, Paris 75005, France; [orcid.org/0000-0001-7362-7849](https://orcid.org/0000-0001-7362-7849)*

Complete contact information is available at: <https://pubs.acs.org/doi/10.1021/acs.jpcc.0c10417>

## Notes

The authors declare no competing financial interest.

## ACKNOWLEDGMENTS

The authors acknowledge the ALISTORE European Research Institute for the funding support of A.T.'s Ph.D. thesis. S.E. acknowledges funding from the EPSRC grant EP/L016087/1. A.A.F. acknowledges the Institut Universitaire de France and the EIG CONCERT Japan (project Car Free) for funding support. This work has received funding from the European Research Council under the European Union's Horizon 2020 research and innovation programme through the projects BATNMR, ARTISTIC and SuPERPORES (Grant nos. 835073, 772873, and 714581, respectively). This research used resources of the Advanced Photon Source, a U.S. Department of Energy (DOE) Office of Science User Facility operated for the DOE Office of Science by Argonne National Laboratory under Contract no. DE AC02 06CH11357.

## REFERENCES

- (1) Abraham, K. M.; Jiang, Z. A Polymer Electrolyte Based Rechargeable Lithium/Oxygen Battery. *J. Electrochem. Soc.* **1996**, *143*, 1–5.
- (2) Ma, Z.; Yuan, X.; Li, L.; Ma, Z. F.; Wilkinson, D. P.; Zhang, L.; Zhang, J. A Review of Cathode Materials and Structures for Rechargeable Lithium–Air Batteries. *Energy Environ. Sci.* **2015**, *8*, 2144–2198.
- (3) Viswanathan, V.; Thygesen, K. S.; Hummelshøj, J. S.; Nørskov, J. K.; Girishkumar, G.; McCloskey, B. D.; Luntz, A. C. Electrical Conductivity in  $\text{Li}_2\text{O}_2$  and Its Role in Determining Capacity Limitations in Non Aqueous  $\text{Li O}_2$  Batteries. *J. Chem. Phys.* **2011**, *135*, 214704.
- (4) Yin, Y.; Torayev, A.; Gaya, C.; Mammeri, Y.; Franco, A. A. Linking the Performances of  $\text{Li-O}_2$  Batteries to Discharge Rate and Electrode and Electrolyte Properties through the Nucleation Mechanism of  $\text{Li}_2\text{O}_2$ . *J. Phys. Chem. C* **2017**, *121*, 19577–19585.
- (5) Luntz, A. C.; Viswanathan, V.; Voss, J.; Varley, J. B.; Nørskov, J. K.; Scheffler, R.; Speidel, A. Tunneling and Polaron Charge Transport through  $\text{Li}_2\text{O}_2$  in  $\text{Li O}_2$  Batteries. *J. Phys. Chem. Lett.* **2013**, *4*, 3494–3499.
- (6) Mitchell, R. R.; Gallant, B. M.; Shao Horn, Y.; Thompson, C. V. Mechanisms of Morphological Evolution of  $\text{Li}_2\text{O}_2$  Particles during Electrochemical Growth. *J. Phys. Chem. Lett.* **2013**, *4*, 1060–1064.
- (7) Zhai, D.; Wang, H. H.; Yang, J.; Lau, K. C.; Li, K.; Amine, K.; Curtiss, L. A. Disproportionation in  $\text{Li O}_2$  Batteries Based on a Large Surface Area Carbon Cathode. *J. Am. Chem. Soc.* **2013**, *135*, 15364–15372.
- (8) Xue, K. H.; McTurk, E.; Johnson, L.; Bruce, P. G.; Franco, A. A. A Comprehensive Model for Non Aqueous Lithium Air Batteries Involving Different Reaction Mechanisms. *J. Electrochem. Soc.* **2015**, *162*, A614–A621.
- (9) Laoire, C. O.; Mukerjee, S.; Abraham, K. M.; Plichta, E. J.; Hendrickson, M. A. Elucidating the Mechanism of Oxygen Reduction for Lithium Air Battery Applications. *J. Phys. Chem. C* **2009**, *113*, 20127–20134.
- (10) Albertus, P.; Girishkumar, G.; McCloskey, B.; Sánchez Carrera, R. S.; Kozinsky, B.; Christensen, J.; Luntz, A. C. Identifying Capacity Limitations in the  $\text{Li/Oxygen}$  Battery Using Experiments and Modeling. *J. Electrochem. Soc.* **2011**, *158*, A343–A351.
- (11) Franco, A. A.; Xue, K. H. Carbon Based Electrodes for Lithium Air Batteries: Scientific and Technological Challenges from a Modeling Perspective. *ECS J. Solid State Sci. Technol.* **2013**, *2*, M3084–M3100.
- (12) Xue, K. H.; Nguyen, T. K.; Franco, A. A. Impact of the Cathode Microstructure on the Discharge Performance of Lithium Air Batteries: A Multiscale Model. *J. Electrochem. Soc.* **2014**, *161*, E3028–E3035.
- (13) Liu, J.; Rahimian, S. K.; Monroe, C. W. Capacity Limiting Mechanisms in  $\text{Li/O}_2$  Batteries. *Phys. Chem. Chem. Phys.* **2016**, *18*, 22840–22851.
- (14) Bardenhagen, I.; Yezerska, O.; Augustin, M.; Fenske, D.; Wittstock, A.; Bäumer, M. In Situ Investigation of Pore Clogging during Discharge of a  $\text{Li/O}_2$  Battery by Electrochemical Impedance Spectroscopy. *J. Power Sources* **2015**, *278*, 255–264.
- (15) Aklalouch, M.; Olivares Marín, M.; Lee, R. C.; Palomino, P.; Enciso, E.; Tonti, D. Mass Transport Control on the Discharge Mechanism in  $\text{Li O}_2$  Batteries Using Carbon Cathodes with Varied Porosity. *ChemSusChem* **2015**, *8*, 3465–3471.
- (16) Ding, N.; Chien, S. W.; Hor, T. S. A.; Lum, R.; Zong, Y.; Liu, Z. Influence of Carbon Pore Size on the Discharge Capacity of  $\text{Li O}_2$  Batteries. *J. Mater. Chem. A* **2014**, *2*, 12433–12441.
- (17) Kim, D. Y.; Kim, M.; Kim, D. W.; Suk, J.; Park, J. J.; Park, O. O.; Kang, Y. Graphene Paper with Controlled Pore Structure for High Performance Cathodes in  $\text{Li-O}_2$  Batteries. *Carbon N. Y.* **2016**, *100*, 265–272.
- (18) Lin, Y.; Moitoso, B.; Martinez Martinez, C.; Walsh, E. D.; Lacey, S. D.; Kim, J. W.; Dai, L.; Hu, L.; Connell, J. W. Ultrahigh Capacity Lithium Oxygen Batteries Enabled by Dry Pressed Holey Graphene Air Cathodes. *Nano Lett.* **2017**, *17*, 3252–3260.
- (19) Yu, R.; Fan, W.; Guo, X.; Dong, S. Highly Ordered and Ultra Long Carbon Nanotube Arrays as Air Cathodes for High Energy Efficiency  $\text{Li Oxygen}$  Batteries. *J. Power Sources* **2016**, *306*, 402–407.
- (20) Aurbach, D.; McCloskey, B. D.; Nazar, L. F.; Bruce, P. G. Advances in Understanding Mechanisms Underpinning Lithium–Air Batteries. *Nat. Energy* **2016**, *1*, 16128.
- (21) Abraham, K. M. Electrolyte Directed Reactions of the Oxygen Electrode in Lithium Air Batteries. *J. Electrochem. Soc.* **2014**, *162*, A3021–A3031.
- (22) Laoire, C. O.; Mukerjee, S.; Abraham, K. M.; Plichta, E. J.; Hendrickson, M. A. Influence of Nonaqueous Solvents on the Electrochemistry of Oxygen in the Rechargeable Lithium–Air Battery. *J. Phys. Chem. C* **2010**, *114*, 9178–9186.
- (23) Johnson, L.; Li, C.; Liu, Z.; Chen, Y.; Freunberger, S. A.; Ashok, P. C.; Praveen, B. B.; Dholakia, K.; Tarascon, J. M.; Bruce, P. G. The Role of  $\text{LiO}_2$  Solubility in  $\text{O}_2$  Reduction in Aprotic Solvents and Its Consequences for  $\text{Li-O}_2$  Batteries. *Nat. Chem.* **2014**, *6*, 1091–1099.
- (24) Burke, C. M.; Pande, V.; Khetan, A.; Viswanathan, V.; McCloskey, B. D. Enhancing Electrochemical Intermediate Solvation through Electrolyte Anion Selection to Increase Nonaqueous  $\text{Li-O}_2$  Battery Capacity. *Proc. Natl. Acad. Sci. U. S. A.* **2015**, *112*, 9293.
- (25) Aetukuri, N. B.; McCloskey, B. D.; García, J. M.; Krupp, L. E.; Viswanathan, V.; Luntz, A. C. Solvating Additives Drive Solution Mediated Electrochemistry and Enhance Toroid Growth in Non Aqueous  $\text{Li O}_2$  Batteries. *Nat. Chem.* **2015**, *7*, 50–56.
- (26) Liu, T.; Frith, J. T.; Kim, G.; Kerber, R. N.; Dubouis, N.; Shao, Y.; Liu, Z.; Magusin, P. C. M. M.; Casford, M. T. L.; Garcia Araez, N.; et al. The Effect of Water on Quinone Redox Mediators in Nonaqueous  $\text{Li O}_2$  Batteries. *J. Am. Chem. Soc.* **2018**, *140*, 1428–1437.
- (27) Lacey, M. J.; Frith, J. T.; Owen, J. R. A Redox Shuttle to Facilitate Oxygen Reduction in the Lithium Air Battery. *Electrochem. Commun.* **2013**, *26*, 74–76.
- (28) Lim, H. D.; Lee, B.; Zheng, Y.; Hong, J.; Kim, J.; Gwon, H.; Ko, Y.; Lee, M.; Cho, K.; Kang, K. Rational Design of Redox Mediators for Advanced  $\text{Li O}_2$  Batteries. *Nat. Energy* **2016**, *1*, 16066.
- (29) Gao, X.; Chen, Y.; Johnson, L.; Bruce, P. G. Promoting Solution Phase Discharge in  $\text{Li O}_2$  Batteries Containing Weakly Solvating Electrolyte Solutions. *Nat. Mater.* **2016**, *15*, 882–888.
- (30) Li, Y.; Zhang, Z.; Duan, D.; Sun, Y.; Wei, G.; Hao, X.; Liu, S.; Han, Y.; Meng, W. The Correlation of the Properties of Pyrrolidinium Based Ionic Liquid Electrolytes with the Discharge–Charge Performances of Rechargeable  $\text{Li-O}_2$  Batteries. *J. Power Sources* **2016**, *329*, 207–215.
- (31) Wu, C.; Li, T.; Liao, C.; Xu, Q.; Cao, Y.; Li, L.; Yang, J. Enhanced Electrochemical Performance of Non Aqueous  $\text{Li-O}_2$  Batteries with Triethylene Glycol Dimethyl Ether Based Electrolyte. *J. Electrochem. Soc.* **2017**, *164*, A1321–A1327.
- (32) Cui, Y.; Wen, Z.; Liang, X.; Lu, Y.; Jin, J.; Wu, M.; Wu, X. A Tubular Polypyrrole Based Air Electrode with Improved  $\text{O}_2$

Diffusivity for Li O<sub>2</sub> Batteries. *Energy Environ. Sci.* **2012**, *5*, 7893–7897.

(33) Li, X.; Huang, J.; Faghri, A. Modeling Study of a Li O<sub>2</sub> Battery with an Active Cathode. *Energy* **2015**, *81*, 489–500.

(34) Wang, F.; Xu, Y. H.; Luo, Z. K.; Pang, Y.; Wu, Q. X.; Liang, C. S.; Chen, J.; Liu, D.; Zhang, X. H. A Dual Pore Carbon Aerogel Based Air Cathode for a Highly Rechargeable Lithium Air Battery. *J. Power Sources* **2014**, *272*, 1061–1071.

(35) Forse, A. C.; Griffin, J. M.; Merlet, C.; Carretero Gonzalez, J.; Raji, A. R. O.; Trease, N. M.; Grey, C. P. Direct Observation of Ion Dynamics in Supercapacitor Electrodes Using in Situ Diffusion NMR Spectroscopy. *Nat. Energy* **2017**, *2*, 16216.

(36) Engelke, S.; Marbella, L. E.; Trease, N. M.; De Volder, M.; Grey, C. P. Three Dimensional Pulsed Field Gradient NMR Measurements of Self Diffusion in Anisotropic Materials for Energy Storage Applications. *Phys. Chem. Chem. Phys.* **2019**, *21*, 4538–4546.

(37) Stallmach, F.; Kärger, J.; Krause, C.; Jeschke, M.; Oberhagemann, U. Evidence of Anisotropic Self Diffusion of Guest Molecules in Nanoporous Materials of MCM 41 Type. *J. Am. Chem. Soc.* **2000**, *122*, 9237–9242.

(38) Kondrashova, D.; Lauerer, A.; Mehlhorn, D.; Jobic, H.; Feldhoff, A.; Thommes, M.; Chakraborty, D.; Gommers, C.; Zecevic, J.; De Jongh, P.; et al. Scale Dependent Diffusion Anisotropy in Nanoporous Silicon. *Sci. Rep.* **2017**, *7*, 1–10.

(39) Torayev, A.; Rucci, A.; Magusin, P. C. M. M.; Demortière, A.; De Andrade, V.; Grey, C. P.; Merlet, C.; Franco, A. A. Stochasticity of Pores Interconnectivity in Li O<sub>2</sub> Batteries and Its Impact on the Variations in Electrochemical Performance. *J. Phys. Chem. Lett.* **2018**, *9*, 791–797.

(40) Torayev, A.; Magusin, P. C. M. M.; Grey, C. P.; Merlet, C.; Franco, A. A. Importance of Incorporating Explicit 3D Resolved Electrode Mesostructures in Li–O<sub>2</sub> Battery Models. *ACS Appl. Energy Mater.* **2018**, *1*, 6433–6441.

(41) Stejskal, E. O.; Tanner, J. E. Spin Diffusion Measurements: Spin Echoes in the Presence of a Time Dependent Field Gradient. *J. Chem. Phys.* **1965**, *42*, 288–292.

(42) Price, W. S. *NMR Studies of Translational Motion*; Cambridge University Press: Cambridge, 2009, DOI: 10.1017/CBO9780511770487.

(43) Chung, D. W.; Ebner, M.; Ely, D. R.; Wood, V.; Edwin García, R. Validity of the Bruggeman Relation for Porous Electrodes. *Modell. Simul. Mater. Sci. Eng.* **2013**, *21*, No. 074009.

(44) De Andrade, V.; Deriy, A.; Wojcik, M. J.; Gürsoy, D.; Shu, D.; Fezzaa, K.; De Carlo, F. Nanoscale 3D Imaging at the Advanced Photon Source. *SPIE Newsroom* **2016**, No. 006461.

(45) Su, Z.; De Andrade, V.; Cretu, S.; Yin, Y.; Wojcik, M. J.; Franco, A. A.; Demortière, A. X Ray Nanocomputed Tomography in Zernike Phase Contrast for Studying 3D Morphology of Li–O<sub>2</sub> Battery Electrode. *ACS Appl. Energy Mater.* **2020**, *3*, 4093–4102.

(46) Gürsoy, D.; De Carlo, F.; Xiao, X.; Jacobsen, C. TomoPy: A Framework for the Analysis of Synchrotron Tomographic Data. *J. Synchrotron Radiat.* **2014**, *21*, 1188–1193.

(47) Pelt, D. M.; Gürsoy, D.; Palenstijn, W. J.; Sijbers, J.; De Carlo, F.; Batenburg, K. J. Integration of TomoPy and the ASTRA Toolbox for Advanced Processing and Reconstruction of Tomographic Synchrotron Data. *J. Synchrotron Radiat.* **2016**, *23*, 842–849.

(48) Arganda Carreras, I.; Kaynig, V.; Rueden, C.; Eliceiri, K. W.; Schindelin, J.; Cardona, A.; Sebastian Seung, H. Trainable Weka Segmentation: A Machine Learning Tool for Microscopy Pixel Classification. *Bioinformatics* **2017**, *33*, 2424–2426.

(49) Cooper, S. J.; Bertei, A.; Shearing, P. R.; Kilner, J. A.; Brandon, N. P. TauFactor: An Open Source Application for Calculating Tortuosity Factors from Tomographic Data. *SoftwareX* **2016**, *5*, 203–210.

(50) Blanquer, G.; Yin, Y.; Quiroga, M. A.; Franco, A. A. Modeling Investigation of the Local Electrochemistry in Lithium O<sub>2</sub> Batteries: A Kinetic Monte Carlo Approach. *J. Electrochem. Soc.* **2016**, *163*, A329–A337.

(51) Reuter, K. First Principles Kinetic Monte Carlo Simulations for Heterogeneous Catalysis: Concepts, Status, and Frontiers. *Modeling and Simulation of Heterogeneous Catalytic Reactions: From the Molecular Process to the Technical System*; John Wiley & Sons, Ltd: 2011; 71–111.

(52) Griffith, L. D.; Sleightholme, A. E. S.; Mansfield, J. F.; Siegel, D. J.; Monroe, C. W. Correlating Li/O<sub>2</sub> Cell Capacity and Product Morphology with Discharge Current. *ACS Appl. Mater. Interfaces* **2015**, *7*, 7670–7678.

(53) Bruggeman, D. A. G. Berechnung Verschiedener Physikalischer Konstanten von Heterogenen Substanzen. I. Dielektrizitätskonstanten Und Leitfähigkeiten Der Mischkörper Aus Isotropen Substanzen. *Ann. Phys.* **1935**, *416*, 636–664.

**Supporting information for**

**Probing and Interpreting the Porosity and Tortuosity**

**Evolution of Li-O<sub>2</sub> Cathodes on Discharge Through a**

**Combined Experimental and Theoretical Approach**

*Amangeldi Torayev,<sup>1,2,3</sup> Simon Engelke,<sup>2,4</sup> Zeliang Su,<sup>1,5</sup> Lauren E. Marbella,<sup>2,6</sup> Vincent De Andrade,<sup>7</sup> Arnaud Demortiere,<sup>1,3,5</sup> Pieter C. M. M. Magusin,<sup>2,3</sup> Céline Merlet,<sup>3,5,8</sup> Alejandro A. Franco,<sup>1,3,5,9</sup> Clare P. Grey<sup>\*2,3</sup>*

<sup>1</sup> *Laboratoire de Réactivité et Chimie des Solides (LRCS), UMR CNRS 7314, Université de Picardie Jules Verne, Hub de l'Energie, 15 Rue Baudelocque, 80039 Amiens, France*

<sup>2</sup> *Department of Chemistry, University of Cambridge, Lensfield Road, Cambridge CB2 1EW, United Kingdom*

<sup>3</sup> *ALISTORE-European Research Institute, FR CNRS 3104, Hub de l'Energie, 15 Rue Baudelocque, 80039 Amiens, France*

<sup>4</sup> *Cambridge Graphene Centre, University of Cambridge, 9 JJ Thomson Avenue, Cambridge, CB3 0FA, UK*

<sup>5</sup> *Réseau sur le Stockage Electrochimique de l'Energie (RS2E), FR CNRS 3459, Hub de l'Energie, 15 Rue Baudelocque, 80039 Amiens, France*

<sup>6</sup> *Department of Chemical Engineering, Columbia University, 500 W 120<sup>th</sup> St, New York, NY 10027, USA*

<sup>7</sup> *X-Ray Science Division, Advanced Photon Source, Argonne National Laboratory, Lemont, USA*

<sup>8</sup> *CIRIMAT, Université de Toulouse, CNRS, Bât. CIRIMAT, 118, route de Narbonne 31062 Toulouse cedex 9, France*

<sup>9</sup> *Institut Universitaire de France, 103 Boulevard Saint-Michel, 75005 Paris, France*

[\\*cpg27@cam.ac.uk](mailto:cpg27@cam.ac.uk)



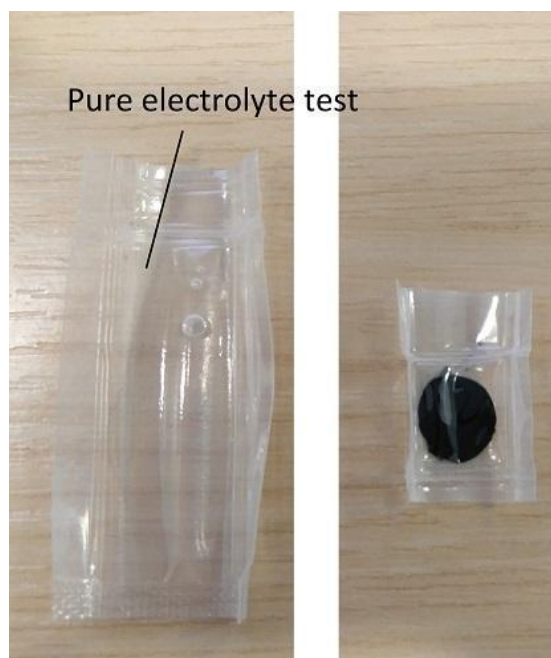


**Figure S1.** Sample holders for PFG-NMR experiments.

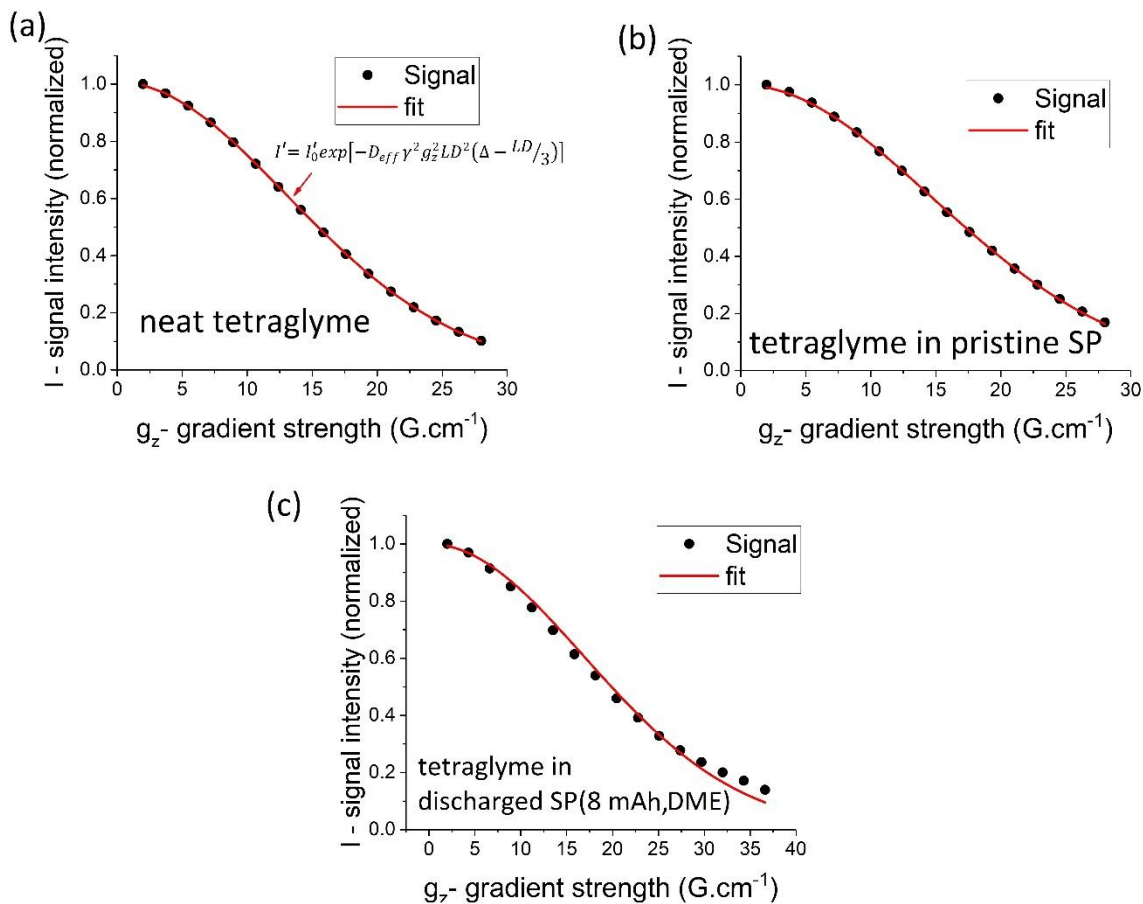


**Figure S2.** PFG-NMR signal intensities recorded for various gradient strengths for (a) neat tetraglyme (b) tetraglyme in pristine Super P electrode (c) tetraglyme in fully discharged (with 0.5 M LiTFSI in DME) Super P.  $\Delta = 1200$  ms;  $\delta = 1$  ms. The signal follows the Stejskal-Tanner equation which describes its intensity as a function of the gradient strength and the diffusion coefficient. The diffusion coefficient is thus extracted by fitting to the acquired signal intensities.

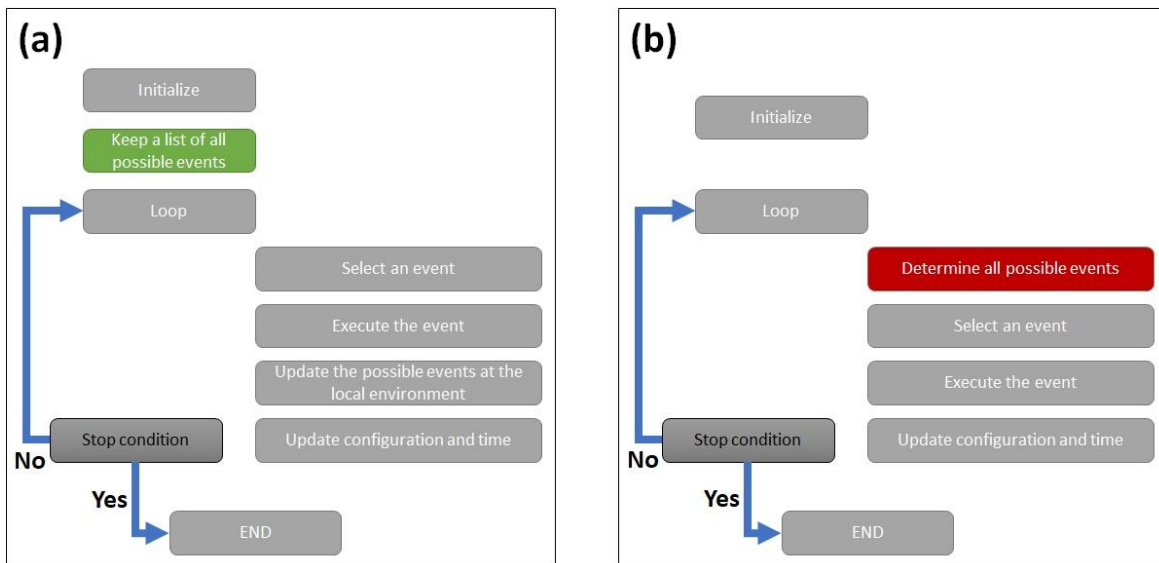


**Figure S3.** *kMC* model flow chart used in (a) this work and (b) literature by Blanquer et al.<sup>1</sup> and Reuter<sup>2</sup>.

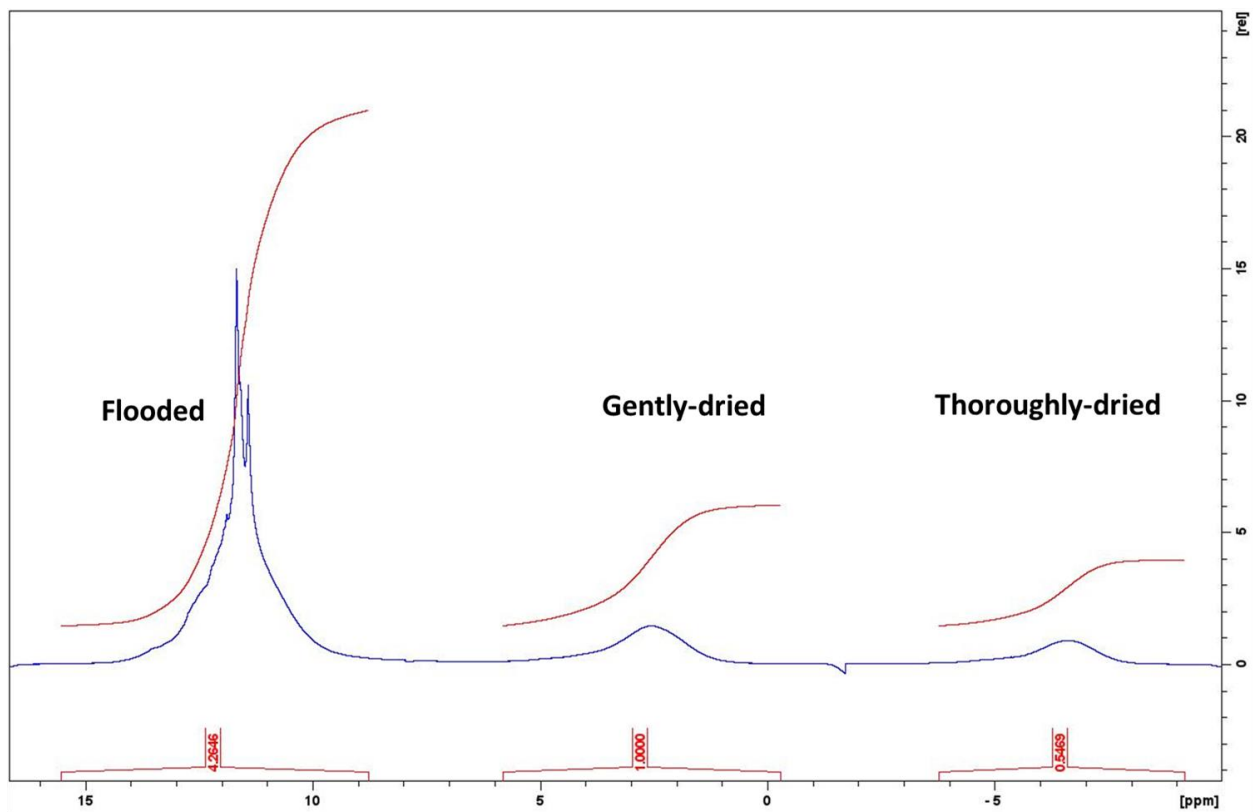


**Figure S4.** Relative solvent quantities for three types of dried electrodes (flooded: 4.26, gently-dried: 1, thoroughly-dried: 0.55).

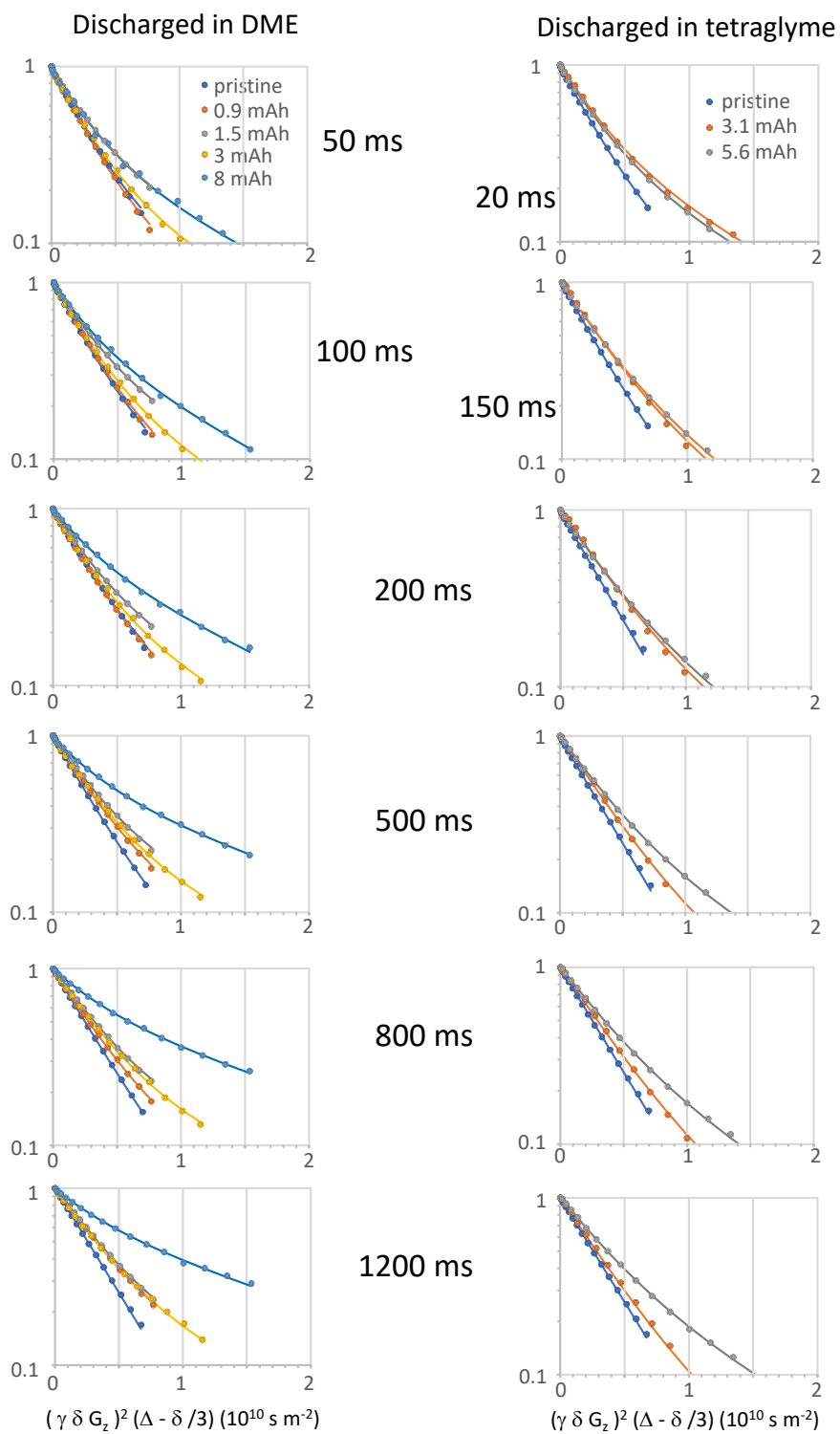


**Figure S5.** PFG echo intensities plotted versus the composed experimental parameter  $\gamma^2 g_z^2 \delta^2 (\Delta - \delta/3)$  (Eq. 2)

		Discharged in DME					Discharged in tetraglyme		
		0 mAh.g <sup>-1</sup>	73 mAh.g <sup>-1</sup>	121 mAh.g <sup>-1</sup>	243 mAh.g <sup>-1</sup>	647 mAh.g <sup>-1</sup>	0 mAh.g <sup>-1</sup>	253 mAh.g <sup>-1</sup>	454 mAh.g <sup>-1</sup>
	20 ms						3.14	2.62	2.71
	50 ms	3.21	3.28	2.73	3.09	2.73			
	100 ms	3.16	3.10	2.65	2.95	2.39			
	150 ms						2.98	2.61	2.52
	200 ms	2.94	2.96	2.60	2.79	2.04	2.81	2.44	2.36
	500 ms	2.91	2.66	2.43	2.56	1.76	2.76	2.50	2.26
	800 ms	2.80	2.58	2.34	2.42	1.49	2.72	2.45	2.14
	1200ms	2.72	2.31	2.24	2.29	1.32	2.71	2.48	2.07

**Table S1.** Weighted average diffusion coefficients  $D_{av} = f_A D_A + f_B D_B$  derived from the bi-exponential model fitting in units of  $10^{-10} \text{ m}^2 \cdot \text{s}^{-1}$ .

### Error analysis:

The error calculation for  $\tau_i/\tau_0$  is calculated as follows. The main relation is

$$D_i = \frac{\varepsilon_i}{\tau_i} D_{bulk}$$

or

$$\tau_0 = \varepsilon_0 \frac{D_{bulk}}{D_0} \quad \text{and} \quad \tau_i = \varepsilon_i \frac{D_{bulk}}{D_i}$$

The relation for  $\tau_i/\tau_0$  is

$$\frac{\tau_i}{\tau_0} = \frac{\varepsilon_i \frac{D_{bulk}}{D_i}}{\varepsilon_0 \frac{D_{bulk}}{D_0}} = \frac{\varepsilon_i \cdot D_{bulk} \cdot D_0}{\varepsilon_0 \cdot D_{bulk} \cdot D_i} = \frac{\varepsilon_i}{\varepsilon_0} \cdot \frac{D_0}{D_i}$$

**Table S2.** Data related to the calculation of the electrode porosity

<b>thickness</b>	300	$\mu\text{m}$
<b>diameter</b>	11	mm
<b>70% Super P</b>	2.26	$\text{g cm}^3$
<b>30% PTFE</b>	2.2	$\text{g cm}^3$
<b>electrode mass</b>	13	$\text{mg cm}^2$
<b>For a 1 cm<sup>2</sup> electrode surface</b>		
<b>electrode volume</b>	$30 \times 10^{-3}$	$\text{cm}^3$
<b>mass</b>	$13 \times 10^{-3}$	g
<b>Super P weight</b>	$9.1 \times 10^{-3}$	g
<b>PTFE weight</b>	$3.9 \times 10^{-3}$	g
<b>SP volume</b>	$4.03 \times 10^{-3}$	$\text{cm}^3$
<b>PTFE volume</b>	$1.77 \times 10^{-3}$	$\text{cm}^3$
<b>solid volume</b>	$5.80 \times 10^{-3}$	$\text{cm}^3$
<b>porosity</b>	0.81	

$$\text{Porosity} = \frac{\text{Electrodevolume} - \text{PTFEvolume} - \text{SPvolume}}{\text{Electrodevolume}}$$

The errors for the diffusion coefficients are obtained from the fitting of the Stejskal-Tanner equation to the PFG-NMR signal as shown in Figure S2. The error for  $D_0$  is 0.49% and the error for  $D_i$  differs for each cell  $i$  ranging from 0.49% for pristine Super P electrode to 32.17% for fully discharged Super P electrode with DME based electrolyte. As all the discharge capacity is coming from the formation of  $\text{Li}_2\text{O}_2$  discharge products, the error in porosity is assumed to be zero. The error for  $\tau_i/\tau_0$  is thus the sum of the maximum errors on  $D_0$  and  $D_i$ .



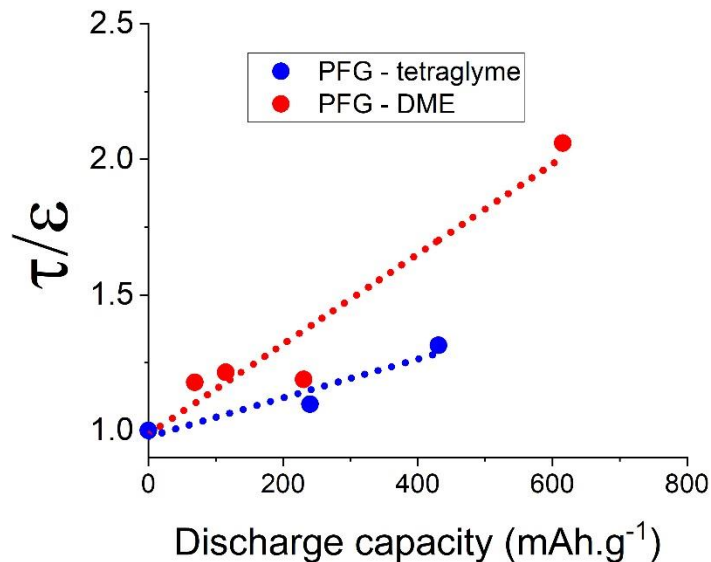


**Figure S6.**  $\frac{\tau}{\varepsilon}$  evolution as a function of depth of discharge.

Calculating the tortuosity evolution along the depth of discharge using the measured diffusion coefficients requires known porosity values ( $\varepsilon$ ) at these discharge points to use the equation below (which corresponds to equation 3 in the main paper):

$$D_{eff} = \frac{\varepsilon}{\tau} D_{bulk} \quad \text{or} \quad \tau = \varepsilon \frac{D_{bulk}}{D_{eff}}$$

In Figure 8 in the main text, the initial porosity is calculated using Table S2 and the porosity change along the depth of discharge is calculated from the capacity by assuming all the discharge product is  $\text{Li}_2\text{O}_2$ . In order to remove any potential errors that arise from the estimate of the porosity,  $\varepsilon$ , we can simply compare  $\tau/\varepsilon$  as a function of state of discharge. Thus the data in Figure 8 in the main text has been replotted in Figure S6 with  $\tau/\varepsilon$  on the y-axis, which simply reflects the ratio of the bulk diffusion and effective diffusion coefficients at each depth of discharge as measured by PFG-NMR. The same trends are observed in Figure S6 and 8, confirming that the trends observed for the tortuosity change are not affected by the porosity assumption.

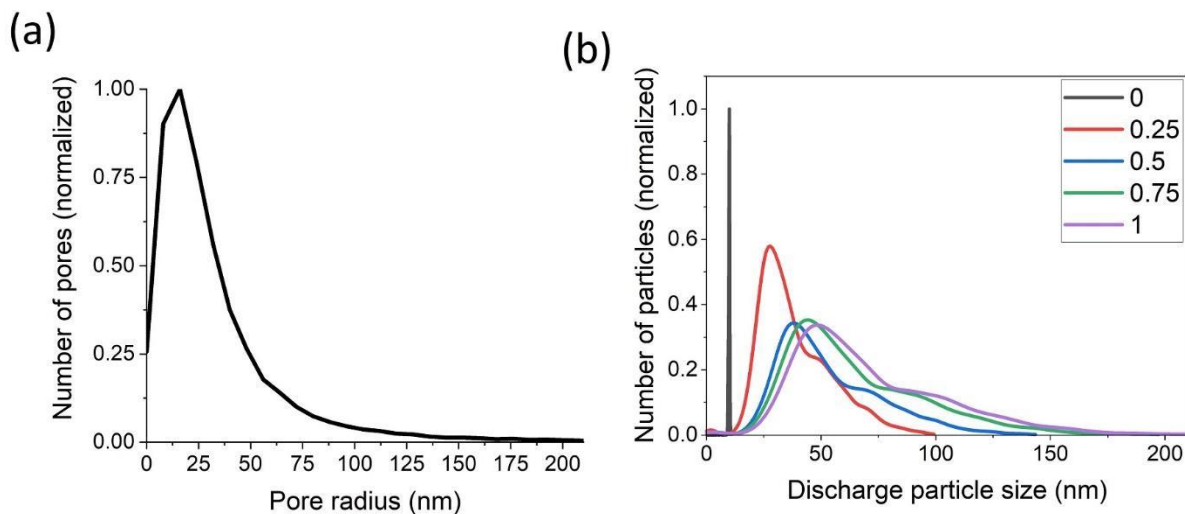


**Figure S7.** (a) Pore size distribution for the Super P carbon used for the PNM model; (b) discharge product size distribution at the end of discharge for 5 different escape factors.

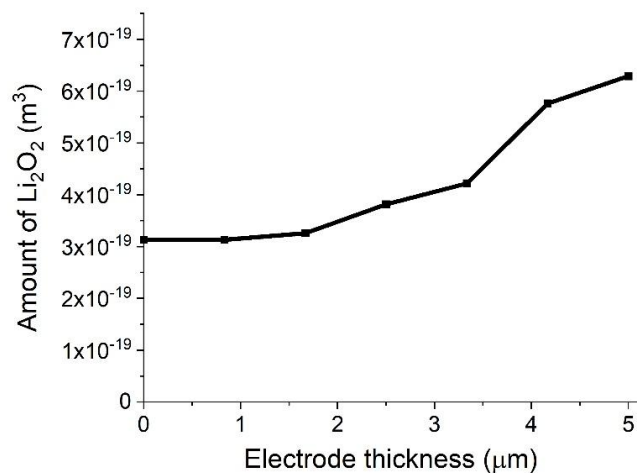


**Figure S8.** Discharge product gradient at the end of discharge for escape factor 0, PNM model

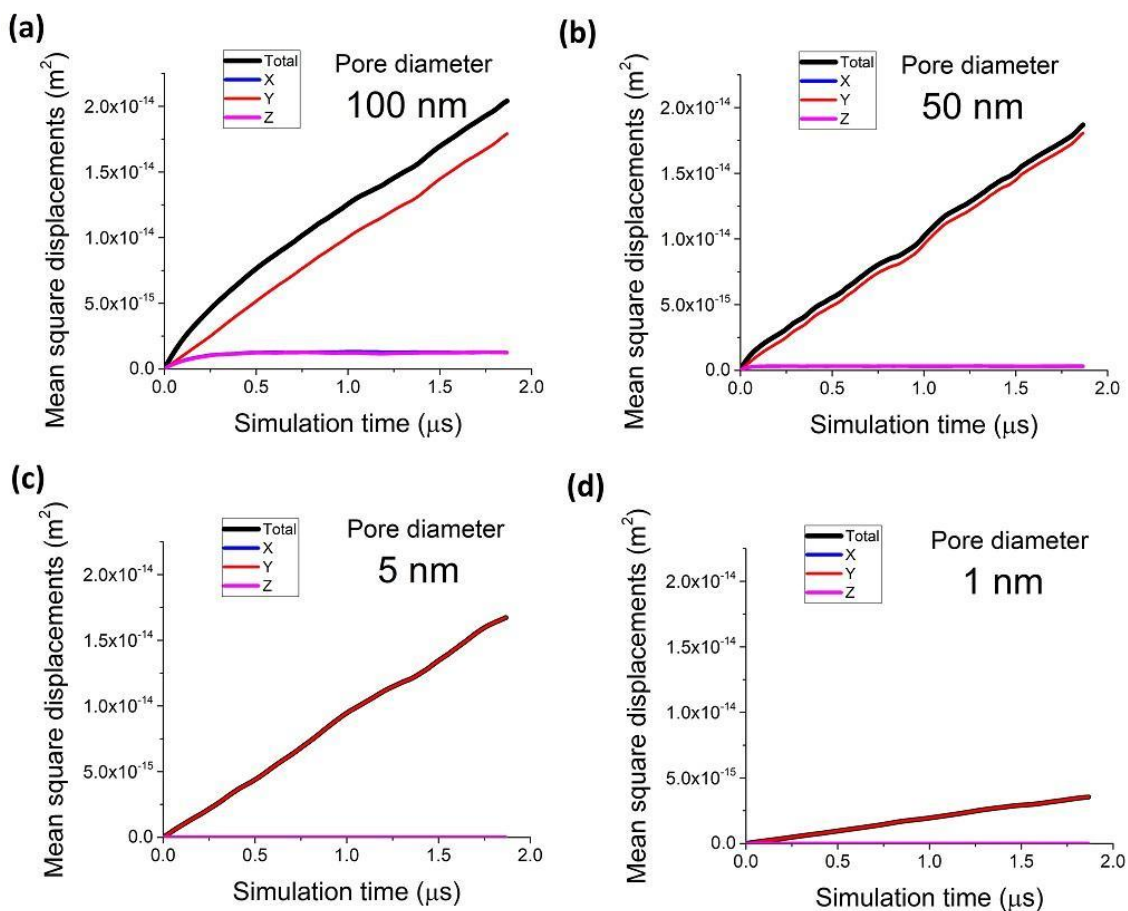


**Figure S9.** MSD curves calculated from kMC trajectories in  $x$ ,  $y$  and  $z$  directions for pores with (a) 100 nm, (b) 50 nm, (c) 5 nm and (d) 1 nm diameters.

Figure S9 shows MSD plots calculated from kMC trajectories. The MSD curves for the  $x$  and  $z$  directions reach a plateau as expected for confined diffusion.<sup>3</sup> On the other hand, the MSD along the  $y$  direction reaches a linear regime without plateau since there are no restrictions along this direction. The diffusion coefficients are obtained by fitting the MSD values in the  $y$  direction. Monte Carlo simulations are stochastic in nature and several simulations are needed to ensure a sufficient statistical accuracy. For each structure, the kMC calculations are repeated three times; and we report the average of those three repetitions.

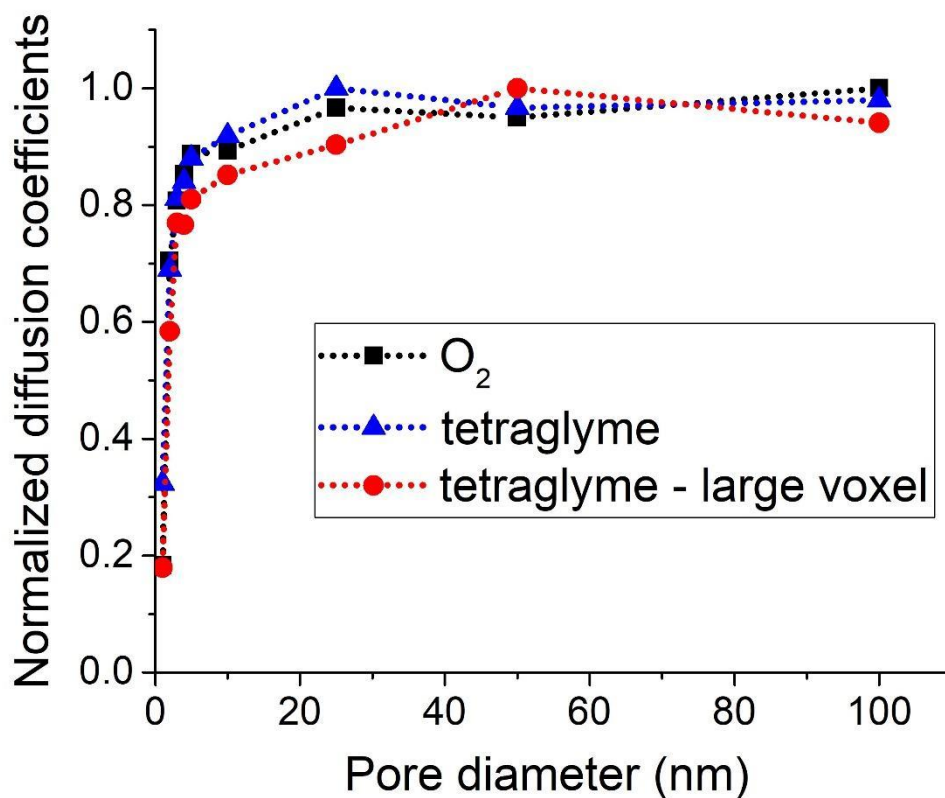


*Figure S10.* O<sub>2</sub> and tetraglyme effective diffusion coefficients calculated using the kMC model for various pore diameters. For the tetraglyme case, two voxel sizes are tested, one with 0.5 nm and another with 0.75 nm (labeled as “tetraglyme - large voxel”).

The marginal differences between diffusion coefficients obtained with different voxel sizes are largely artifacts of the model which arise because of the mapping of a cylinder with square voxels. When the voxel size gets smaller, it maps more area within the cross-section of the cylinder. Thus, when the molecule size gets larger (which corresponds to larger voxels), the molecule has marginally less area to diffuse within.

## REFERENCES

- (1) Blanquer, G.; Yin, Y.; Quiroga, M. A.; Franco, A. A. Modeling Investigation of the Local Electrochemistry in Lithium-O<sub>2</sub> Batteries: A Kinetic Monte Carlo Approach. *J. Electrochem. Soc.* **2016**, *163*, A329–A337.
- (2) Reuter, K. First-Principles Kinetic Monte Carlo Simulations for Heterogeneous Catalysis: Concepts, Status, and Frontiers. *Model. Simul. Heterog. Catal. React.* **2011**, 71–111.
- (3) Bickel, T. A Note on Confined Diffusion. *Phys. A Stat. Mech. its Appl.* **2007**, *377*, 24–32.